Nonlinear Transformed Low-Rank Quaternion Tensor Total Variation for Multidimensional Color Image Completion

Liqiao Yang, Yexun Hu, *Graduate Student Member, IEEE*, Tai-Xiang Jiang, *Member, IEEE*, Yimin Wei, Guisong Liu, *Member, IEEE*, and Michael K. Ng, *Senior Member, IEEE*

***Abstract*—Completing multidimensional color images is a fundamental challenge in image processing and computer vision. However, some tensor-based methods often treat RGB channels as independent modes, thereby neglecting their intrinsic correlations. To address this limitation, we represent RGB values as pure quaternions and organize them into a quaternion tensor for holistic modeling that preserves chromatic relationships. To better capture the nonlinear characteristics inherent in visual data and to improve the compactness of low-rank representations, we propose a nonlinear transformation within the quaternion domain. This design enables more expressive modeling compared to conventional linear approaches. In addition, we introduce two novel regularization terms that jointly encode global low-rankness and local smoothness, with the nonlinear transformation further enhancing the exploitation of structural priors. The overall model is optimized via a nonlinear alternating direction method of multipliers (ADMM), with theoretical guarantees of convergence. Extensive experiments on several datasets demonstrate that the proposed method significantly outperforms state-of-the-art low-rank tensor and quaternion tensor recovery techniques in multidimensional color image completion tasks.**

***Index Terms*—Quaternion tensor, RGB channels, low-rank, local smoothness, nonlinear transformation.**

Received 23 July 2025; revised 14 November 2025; accepted 15 February 2026. Date of publication 5 March 2026; date of current version 11 March 2026. This work was supported in part by Sichuan Science and Technology Program under Grant 2024ZYD0147, in part by the Natural Science Foundation of Xinjiang Uygur Autonomous Region under Grant 2024D01A18, in part by the GDSTC Guangdong and Hong Kong Universities "1+1+1" Joint Research Collaboration Scheme under Grant UICR0800008-24, in part by the National Key Research and Development Program of China under Grant 2024YFE0202900, in part by the RGC GRF under Grant 12300125, in part by the Joint NSFC and RGC under Grant N-HKU769/21, in part by the National Natural Science Foundation of China under Grant U24A2001, in part by Guanghua Talent Project, in part by the Graduate Representative Achievement Cultivation Project of Southwest University of Finance and Economics under Grant JGS2024069, in part by the Chengdu Science and Technology Program under Grant 2025-YF- 00009-RC, and in part by the China Postdoctoral Science Foundation under Grant 2025M783136. The associate editor coordinating the review of this article and approving it for publication was Dr. Zheng Wang. *(Corresponding author: Tai-Xiang Jiang.)*

Liqiao Yang, Yexun Hu, Tai-Xiang Jiang, and Guisong Liu are with the School of Computing and Artificial Intelligence, Southwestern University of Finance and Economics, Chengdu, Sichuan 610074, China, and also with the Kash Institute of Electronics and Information Industry, Kashgar, Xinjiang 844000, China (e-mail: liqiaoyoung@163.com; huyexun2022@163.com; taixiangjiang@gmail.com; gliu@swufe.edu.cn).

Yimin Wei is with the School of Mathematical Sciences and Key Laboratory of Mathematics for Nonlinear Sciences, Fudan University, Shanghai 200433, China (e-mail: ymwei@fudan.edu.cn).

Michael K. Ng is with the Department of Mathematics, Hong Kong Baptist University, Kowloon Tong, Hong Kong (e-mail: michael-ng@hkbu.edu.hk).

This article has supplementary downloadable material available at https://doi.org/10.1109/TIP.2026.3666728, provided by the authors.

Digital Object Identifier 10.1109/TIP.2026.3666728

I. Introduction

MULTIDIMENSIONAL color images, such as color videos, light field images, and multi-view images, are central to many applications in modern image processing and computer vision. These data structures extend beyond spatial dimensions (width and height) to include additional modes like time or viewing angle. However, during acquisition or transmission, this data is often corrupted by missing entries due to sensor failure, limited sampling, or communication errors. Recovering the complete image from these incomplete observations constitutes a challenging inverse problem that has garnered significant research interest [1], [2], [3]. This is part of a broader field of image and video restoration, which has seen recent advances in related video-specific tasks such as multi-scale deraining [4], remote sensing video super-resolution [5], and temporally coherent video dehazing [6].

To faithfully preserve the intrinsic correlation among the red (R), green (G), and blue (B) color channels, quaternion algebra has emerged as a powerful and natural representation. In this paradigm, the three channel values of a pixel are encoded as the three imaginary components of a pure quaternion, as illustrated in Fig. 1 (top). This holistic treatment of color has proven superior to treating channels independently or converting to grayscale [7], leading to successful applications in color image denoising [8], inpainting [9], and video recovery [10].

The extension of this paradigm to multidimensional color images has led to the development of quaternion tensor (QT) models. A QT naturally represents a multidimensional color image by stacking quaternion matrices (e.g., color image frames) along a third or higher-order mode, as shown in Fig. 1 (bottom). Although quaternion-based models inherently capture the relationships among RGB channels, their application to multidimensional color image modeling remains relatively underexplored. Existing QT completion methods have primarily focused on extending real-valued tensor low-rank linear models. This has spurred the definition of various QT ranks, including those based on Tucker [11], tensor train [12], and tensor ring [13] decompositions. More recently, a transform-based QT product framework gave rise to the quaternion tensor singular value decomposition (TQt-SVD) and the corresponding TQt-rank [14].

Despite these advances, two fundamental challenges persist in multidimensional color image completion. First, while real-valued tensor models are prevalent [15], [16], they typically stack color channels along a tensor mode, disrupting

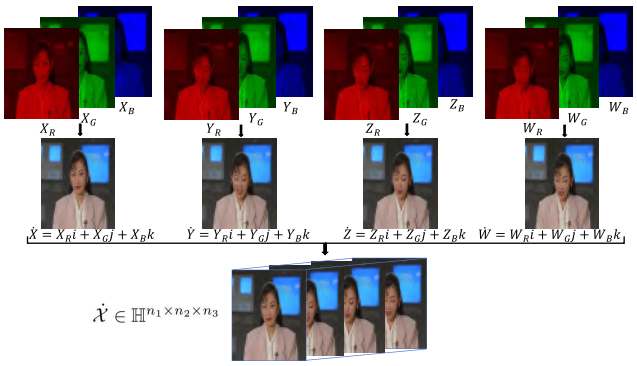

Fig. 1. The pure quaternion tensor representation of a color video.

the inherent color structure. Nonetheless, their use of hybrid regularization, which combines global low-rankness with local priors like TV-based smoothness [3], [17], [18], [19] or sparsity [20], has been highly effective. This brings in an insight that can be adapted to the quaternion domain. Second, real-world visual data often exhibits complex nonlinear structures arising from motion, illumination changes, and object interactions, which cannot be adequately captured by the aforementioned linear QT (or real-valued tensor) models. Although recent works have explored nonlinear transformations in real-valued tensor recovery [21], [22], [23], [24], their integration into the quaternion tensor framework, along with the associated optimization and convergence analysis, remains challenging.

To address these limitations, this paper proposes novel nonlinear transformed quaternion tensor total variation (NTQTTV) methods for multidimensional color image completion. To visually motivate our approach, Fig. 2 analyzes the underlying structure of a sample color video (*news*) and demonstrates the efficacy of our proposed priors. As shown in Fig. 2-(a) and 2-(c), the histogram of the differenced quaternion tensor exhibits a sharp peak centered at zero, indicating strong gradient sparsity. This supports the use of total variation regularization to enforce local smoothness. In parallel, the singular values of the transformed tensor decay rapidly, confirming its global low-rank nature. These observations justify the integration of both sparsity and low-rank priors in our regularization framework. The key advantage of the proposed nonlinear framework is quantitatively demonstrated by the accumulated energy ratio (AccEgy) plots in Fig. 2-(b) and 2-(d), which evaluate the compactness of the low-rank representation. AccEgy is defined as $\text{AccEgy} = \frac{\sum_{i=1}^{k} \sigma_i^2}{\sum_j \sigma_j^2}$, where σ_i is the i-th singular value. A faster-rising curve indicates that more energy is concentrated in fewer singular values. As shown, our proposed NTQTTV2 model significantly outperforms its linear counterpart (linear quaternion tensor total variation, LQTTV), and real-valued state-of-the-art tensor methods, including the nonlinear transformed tensor nuclear norm (NTTNN) [21] and tensor-correlated total variation (t-CTV) [3]. Similarly, the multi-mode analysis reveals that NTQTTV1 consistently captures more energy than the linear LQTTV across all modes. This provides strong empirical evidence that our nonlinear transformation maps the data to a feature space where the low-rank structure is substantially more pronounced, justifying its integration with a QTTV regularizer.

Our approach makes the following key contributions:

- Two novel multidimensional color image completion models are established with two novel regularizers, termed nonlinear transformed quaternion tensor total variation 1 and 2 (NTQTTV1 and NTQTTV2), respectively. Both of these regularizers simultaneously capture nonlinear features, global low-rankness, and local smoothness. Meanwhile, by leveraging the quaternion algebra, our model effectively preserves the intrinsic correlations among RGB channels.
- To address the optimization challenges posed by the nonlinear regularizers, we develop an efficient algorithm based on a local linear approximation strategy. At each iteration, the nonlinear transform is linearized, resulting in a sequence of convex subproblems that can be effectively solved using the alternating direction method of multipliers (ADMM). We further provide a rigorous theoretical analysis to ensure the convergence of the proposed algorithm.
- Extensive experiments on two types of multidimensional color images, including real color video data and light field image completion tasks, illustrate that the proposed methods achieve state-of-the-art performance, outperforming a wide range of competing tensor completion techniques.

The remainder of this paper is organized as follows. Section II reviews essential preliminaries on quaternions and tensors. Section III details the proposed nonlinear model and the optimization algorithm. Section IV presents the experimental results that validate the effectiveness and superiority of our method. Finally, Section V concludes the paper, with the convergence analysis provided in the Supplementary Material.

II. Notations and Preliminaries

The primary notations used throughout this paper are summarized in Table I. Then, we introduce the preliminaries for quaternions and quaternion tensors.

A quaternion [25] $\dot{q} \in \mathbb{H}$ is a hypercomplex number defined as $\dot{q} = q_0 + q_1\mathbf{i} + q_2\mathbf{j} + q_3\mathbf{k}$, where $q_0, q_1, q_2, q_3 \in \mathbb{R}$ and the imaginary units $\mathbf{i}, \mathbf{j}, \mathbf{k}$ follow Hamilton's rules: $\mathbf{i}^2 = \mathbf{j}^2 = \mathbf{k}^2 = \mathbf{ijk} = -1$. The real part is $\Re(\dot{q}) = q_0$ and the vector (imaginary) part is $\Im(\dot{q}) = q_1\mathbf{i} + q_2\mathbf{j} + q_3\mathbf{k}$. Its conjugate is $\dot{q}^* = q_0 - q_1\mathbf{i} - q_2\mathbf{j} - q_3\mathbf{k}$, and its modulus is $|\dot{q}| = \sqrt{\dot{q}^*\dot{q}} = \sqrt{q_0^2 + q_1^2 + q_2^2 + q_3^2}$.

Definition 1 (Quaternion Tensor [11]): A multidimensional array or a k-th order tensor is defined as a quaternion tensor when its entries are quaternions. Specifically, quaternion tensor $\dot{\mathcal{A}} = (\dot{a}_{i_1 i_2 \ldots i_k}) \in \mathbb{H}^{n_1 \times n_2 \times \cdots \times n_k}$ is formulated as $\dot{\mathcal{A}} = \mathcal{A}_0 + \mathcal{A}_1\mathbf{i} + \mathcal{A}_2\mathbf{j} + \mathcal{A}_3\mathbf{k}$, where $\mathcal{A}_n \in \mathbb{R}^{n_1 \times n_2 \times \cdots \times n_k} (n = 0, 1, 2, 3)$ are real-valued tensors. If $\mathcal{A}_0$ is a zero tensor, $\dot{\mathcal{A}}$ is termed a pure quaternion tensor.

Recently, a generalized product for quaternion tensors was introduced in [14], leading to a corresponding tensor singular value decomposition (TQt-SVD).

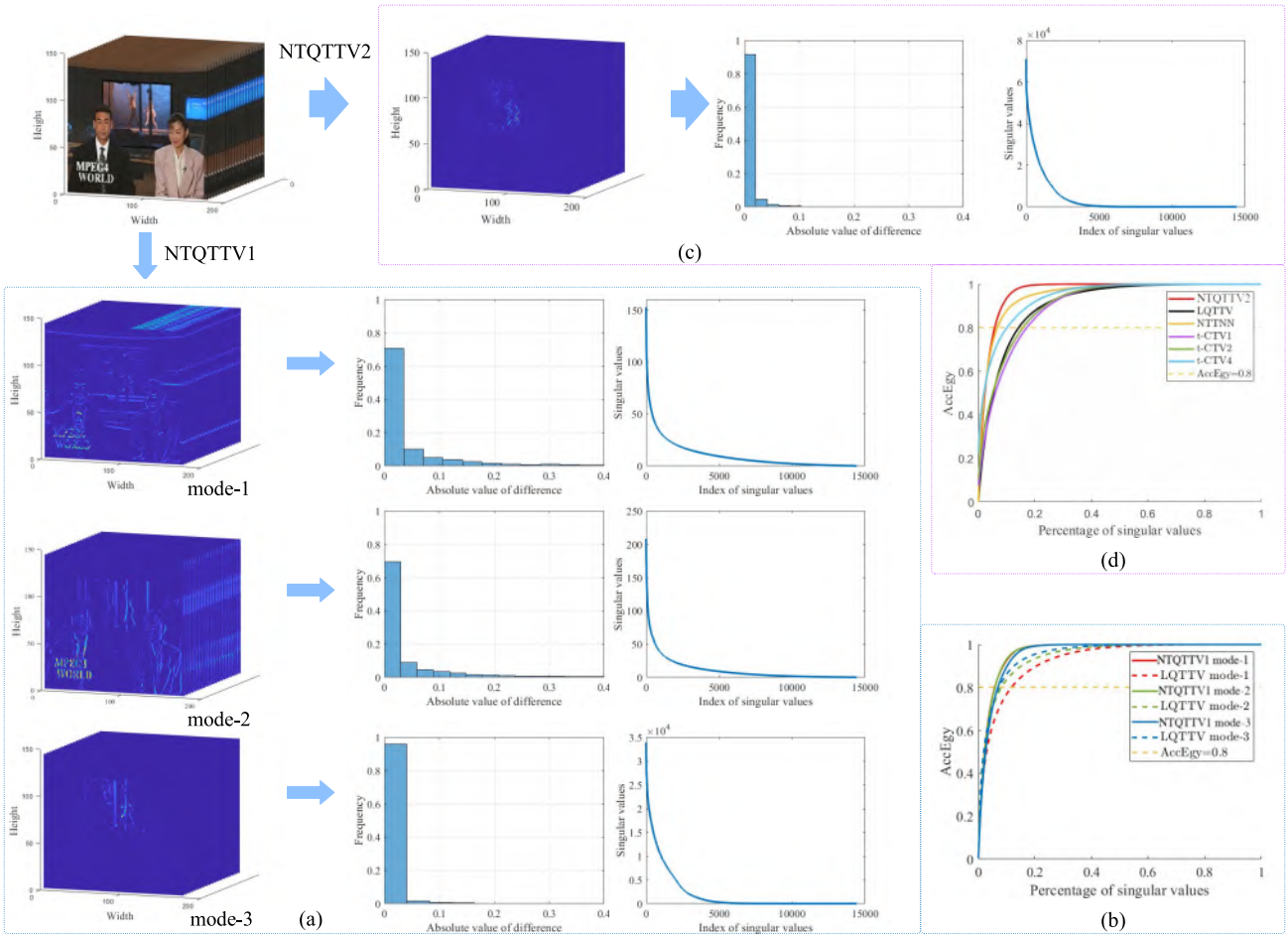

Fig. 2. (a) And (c): Illustration of the joint low-rankness and smoothness structures encoded in correlated gradient quaternion tensors. (b) and (d): The AccEgy of the transformed tensor or quaternion tensor computed under the t-SVD or TQt-SVD framework.

Definition 2 ($\star_{QT}$-Product [14]): Let $\dot{\mathcal{A}} \in \mathbb{H}^{n_1 \times l \times n_3 \times \ldots \times n_k}$ and $\dot{\mathcal{B}} \in \mathbb{H}^{l \times n_2 \times n_3 \times \ldots \times n_k}$ be two k-th order ($k \geq 3$) quaternion tensors. Let $\mathcal{L}$ be an invertible linear transform defined by a set of invertible matrices $\{\dot{\mathbf{Q}}_m \in \mathbb{H}^{n_m \times n_m}\}_{m=3}^{k}$, such that $\mathcal{L}(\cdot) = (\cdot) \times_3 \dot{\mathbf{Q}}_3 \times_4 \cdots \times_k \dot{\mathbf{Q}}_k$. The $\star_{QT}$-product is defined as:

$$\dot{\mathcal{T}} = \dot{\mathcal{A}} \star_{QT} \dot{\mathcal{B}} = \mathcal{L}^{-1}\big(\mathcal{L}(\dot{\mathcal{A}}) \star_{QF} \mathcal{L}(\dot{\mathcal{B}})\big), \tag{1}$$

where $\star_{QF}$ denotes the facewise product, such that for any frontal slice index $(i_3, \ldots, i_k)$, $(\mathcal{L}(\dot{\mathcal{A}}) \star_{QF} \mathcal{L}(\dot{\mathcal{B}}))(:, :, i_3, \ldots, i_k) = \mathcal{L}(\dot{\mathcal{A}})(:, :, i_3, \ldots, i_k)\mathcal{L}(\dot{\mathcal{B}})(:, :, i_3, \ldots, i_k)$.

Remark 1: In this work, the invertible transform $\mathcal{L}$ is implemented using the quaternion discrete cosine transform (QDCT) along modes 3 to k. The choice of QDCT over other possible transforms, such as the quaternion discrete Fourier transform (QDFT), is motivated by its superior energy compaction capability for natural high-dimensional color data. This property means the QDCT is highly effective at capturing the low-frequency components that define the data's core structure. This advantage stems from their different boundary assumptions: the QDFT assumes a periodic signal, which often creates artificial discontinuities at the data's edges, whereas the QDCT assumes symmetric (reflective) boundaries, which maintains smoothness and is a far better fit for natural data. This makes the QDCT a natural fit for our framework, as its efficiency in compressing spatially smooth data complements our total variation regularizer, and its ability to reveal a more compact low-rank structure is better suited for our quaternion tensor nuclear norm (QTNN) objective. The transformed tensor is denoted as $\hat{\dot{\mathcal{A}}} = \mathcal{L}(\dot{\mathcal{A}})$.

This $\star_{QT}$-product allows for a generalized SVD for quaternion tensors.

Theorem 1 (TQt-SVD [14]): For any quaternion tensor $\dot{\mathcal{T}} \in \mathbb{H}^{n_1 \times n_2 \times \cdots \times n_k}$, its TQt-SVD is given by:

$$\dot{\mathcal{T}} = \dot{\mathcal{U}} \star_{QT} \dot{\mathcal{D}} \star_{QT} \dot{\mathcal{V}}^H,$$

where $\dot{\mathcal{U}} \in \mathbb{H}^{n_1 \times n_1 \times \cdots \times n_k}$ and $\dot{\mathcal{V}} \in \mathbb{H}^{n_2 \times n_2 \times \cdots \times n_k}$ are unitary quaternion tensors, and $\dot{\mathcal{D}} \in \mathbb{H}^{n_1 \times n_2 \times \cdots \times n_k}$ is an f-diagonal tensor, meaning its frontal slices are diagonal matrices.

Based on TQt-SVD, the TQt-rank and its convex surrogate, the quaternion tensor nuclear norm (QTNN), are defined.

Definition 3 (TQt-rank [14]): Let the TQt-SVD of $\dot{\mathcal{T}}$ be $\dot{\mathcal{U}} \star_{QT} \dot{\mathcal{D}} \star_{QT} \dot{\mathcal{V}}^H$. The TQt-rank of $\dot{\mathcal{T}}$ is the number of non-zero tubes in the f-diagonal tensor $\dot{\mathcal{D}}$:

$$\operatorname{rank}_{TQt}(\dot{\mathcal{T}}) := \#\big\{i \mid \|\dot{\mathcal{D}}(i, i, :, \ldots, :)\|_F > 0\big\},$$

where $i \in \{1, \ldots, \min(n_1, n_2)\}$. The i-th singular value of $\dot{\mathcal{T}}$ is defined as $\sigma_i(\dot{\mathcal{T}}) := \|\dot{\mathcal{D}}(i, i, :, \ldots, :)\|_F$.

TABLE I
A SUMMARY OF KEY NOTATIONS

Notation	Description
$a, \mathbf{A}, \mathcal{A}$	A scalar, matrix, and tensor in the real domain $\mathbb{R}$.
$\dot{a}, \dot{\mathbf{A}}, \dot{\mathcal{A}}$	A quaternion scalar, matrix, and tensor in the quaternion domain $\mathbb{H}$.
$\Re(\dot{q}), \Im(\dot{q})$	The real part and vector (imaginary) part of a quaternion $\dot{q}$.
$\dot{q}^*$	The conjugate of a quaternion $\dot{q}$.
$\lvert\dot{q}\rvert$	The modulus (absolute value) of a quaternion $\dot{q}$ and $\lvert\dot{a}\rvert^2 = \dot{a}^*\dot{a} = a_1^2 + a_2^2 + a_3^2 + a_4^2$
$\dot{a}_{i_1 i_2 \ldots i_k}$	The $(i_1, i_2, \ldots, i_k)$-th element of tensor $\dot{\mathcal{A}}$.
$\dot{\mathcal{A}}(:,:,i_3,\cdots,i_k)$	the frontal slice of $\dot{\mathcal{A}} \in \mathbb{H}^{n_1 \times n_2 \times \cdots \times n_k}$, where $i_j = 1, \cdots, n_j$, $j = 3, \cdots, k$
$\dot{\mathcal{A}}^{(j)}$ or $\dot{\mathcal{A}}(:,:,j)$	The j-th frontal slice of a 3rd-order tensor $\dot{\mathcal{A}}$.
$(\cdot)^T, (\cdot)^H, (\cdot)^{-1}$	Transpose, conjugate transpose (Hermitian), and inverse operators.
∇_d	The finite difference operator along the d-th dimension.
$\lVert\cdot\rVert_*, \lVert\cdot\rVert_F$	The nuclear norm and Frobenius norm.
$\text{unfold}_j(\cdot)$	Mode-j unfolding: $\mathbb{H}^{n_1 \times \cdots \times n_k} \to \mathbb{H}^{n_j \times (n_1 \cdots n_{j-1} n_{j+1} \cdots n_k)}$.
$\text{fold}_j(\cdot)$	Mode-j folding, the inverse operation of $\text{unfold}_j(\cdot)$.
$\dot{\mathcal{X}} \times_j \dot{\mathbf{A}}$	The mode-j product, defined as $\text{fold}_j(\dot{\mathbf{A}}\,\text{unfold}_j(\dot{\mathcal{X}}))$.
$\star_{QT}$	The quaternion tensor product defined in Def. 2.

Definition 4 (QTNN): The quaternion tensor nuclear norm (QTNN) of $\dot{\mathcal{T}} \in \mathbb{H}^{n_1 \times n_2 \times \cdots \times n_k}$, denoted $\lVert\dot{\mathcal{T}}\rVert_{\text{QTNN}}$, is the sum of the matrix nuclear norms of the frontal slices of the transformed tensor $\hat{\dot{\mathcal{T}}} = \mathcal{L}(\dot{\mathcal{T}})$. Letting $N_3 = \prod_{m=3}^{k} n_m$ and reshaping $\hat{\dot{\mathcal{T}}}$ to be of size $n_1 \times n_2 \times N_3$, the QTNN is:

$$\lVert\dot{\mathcal{T}}\rVert_{\text{QTNN}} := \sum_{i=1}^{N_3} \lVert\tilde{\dot{\mathcal{T}}}^{(i)}\rVert_*, \tag{2}$$

where $\tilde{\dot{\mathcal{T}}} = \text{reshape}(\mathcal{L}(\hat{\dot{\mathcal{T}}}), [n_1, n_2, n_3 n_4 \cdots n_k])$.

For a comprehensive background on quaternion algebra and tensors, we refer the reader to [11], [14], [26], and [27].

III. THE PROPOSED METHOD

In this section, we introduce the nonlinear transformed quaternion tensor total variation regularization methods for multidimensional color image recovery. Specifically, Section III-A presents the design of the proposed regularization terms and formulates corresponding multidimensional color image completion models. Section III-B describes the corresponding nonlinear optimization algorithm based on the ADMM framework. We begin by outlining the core mechanism of our model, followed by its mathematical formulation.

Our model combines three key principles to overcome the limitations of prior approaches. First, the quaternion representation is the foundation, ensuring the preservation of color correlations across channels and preventing artifacts. Second, a nonlinear transformation maps the data into a feature space where its underlying low-rank structure is more clearly captured. Lastly, a unified regularizer operates on this enhanced representation, combining two complementary priors: the global low-rank prior (QTNN) to capture the dominant low-frequency scene structure, with the local smoothness prior (TV) to preserve sparse high-frequency details such as sharp edges. This integration of a robust color model, a structure-enhancing transformation, and a hybrid regularizer is the core advantage of our approach.

A. Proposed Models

To explore the inner nonlinear structure of multidimensional color images, we define the nonlinear activation function first. Let $\dot{\mathcal{X}} = \mathcal{X}_0 + \mathcal{X}_1\mathbf{i} + \mathcal{X}_2\mathbf{j} + \mathcal{X}_3\mathbf{k}$, the nonlinear transform is defined component-wise as

$$\psi(\dot{\mathcal{X}}) = \phi(\mathcal{X}_0) + \mathbf{i}\phi(\mathcal{X}_1) + \mathbf{j}\phi(\mathcal{X}_2) + \mathbf{k}\phi(\mathcal{X}_3),$$

where $\phi(\cdot)$ is a nonlinear function mapping from $\mathbb{R}$ to $\mathbb{R}$.

This strategy is inspired by the success of single-layer orthogonal neural networks in the real domain [28] and the use of split activation functions in quaternion neural networks [29]. Several common choices for $\phi(\cdot)$ include the Hyperbolic tangent (tanh), Sigmoid function, and Leaky ReLU [30]. In this work, we empirically adopt tanh, which is defined as

$$\phi(x) = \tanh(x) = \frac{e^x - e^{-x}}{e^x + e^{-x}},$$

as the nonlinear activation function based on the ablation study (See Table V in the experimental part).

In addition to low-rankness, smoothness serves as a critical prior for the recovery of multidimensional color images, particularly in preserving local structural continuity. Motivated by the unified regularization approach proposed in [3], which integrates low-rankness and smoothness into a single total variation norm for real-valued tensors, we extend this idea to quaternion tensors. Specifically, we design a quaternion tensor total variation regularizer that simultaneously encodes global low-rank structure and local directional smoothness within one norm. This unified norm naturally leverages the nonlinear quaternion transform, enabling a compact and effective characterization of the intrinsic properties of multidimensional color data while preserving the algebraic relationships among RGB channels.

To achieve this, we formally define the nonlinear transformed quaternion tensor total variation norms. First, we consider the total variation along a specific mode of the nonlinear transformed quaternion, which is computed by

$$\nabla_d(\psi(\dot{\mathcal{X}})) := \psi(\dot{\mathcal{X}}) \times_d \mathbf{D}_{n_d}, \tag{3}$$

where $\mathbf{D}_{n_d}$ is a row circulant matrix of $(-w_{n_d}, w_{n_d}, 0, \ldots, 0)$, and $w_{n_d} \in \mathbb{R}^+$. The use of a circulant matrix formulation mathematically enforces circular boundary conditions, a standard approach that enables the efficient use of the Fast Fourier Transform (FFT) for solving the resulting optimization subproblems. Then, we provide the first nonlinear transformed quaternion tensor total variation norm (NTQTTV1) as follows.

Definition 5 (NTQTTV1): For $\dot{\mathcal{X}} \in \mathbb{H}^{n_1 \times n_2 \times \cdots \times n_k}$, and let Γ denote a predefined set of modes (i.e., directions) along which $\dot{\mathcal{X}}$ is assumed to exhibit coupled low-rank and smooth

TABLE II
THE DIFFERENCES AND RELATIONSHIPS OF THE RELATED METHODS

Method	Domain	Low-Rank Prior Description	Nonlinear Transform	Smoothness (TV-based)	Sparsity Prior	Theory
TNN-TV [19]	Real	Nuclear norm (tensor SVD-based)	✗	✓	✗	✓
SNN-TV [17]	Real	Nuclear norm (Tucker-based)	✗	✓	✗	✗
t-CTV [3]	Real	t-CTV for inducing low-rankness	✗	✓	✗	✓
TC-NTTNN [21]	Real	Nuclear norm (tensor SVD-based)	✓	✗	✗	✓
GTNN [20]	Real	Nuclear norm (tensor SVD-based)	✗	✗	✓	✓
LRQTC [11]	Quaternion	Nuclear norm (Tucker-based)	✗	✗	✗	✗
QT-RNNS1 [32]	Quaternion	Nuclear norm (TQt-SVD-based)	✗	✗	✓	✓
NTQTTV (Ours)	**Quaternion**	**QTNN (TQt-SVD-based)**	✓	✓	✗	✓

TABLE III
PERFORMANCE (PSNR/ASSIM VALUES) AND AVERAGE RUNNING TIME IN SECONDS (S) OF DIFFERENT ALGORITHMS FOR 8 COLOR VIDEO RECOVERY. THE BEST NUMERICAL RESULTS ARE HIGHLIGHTED IN BOLD, AND THE SECOND-BEST RESULTS ARE UNDERLINED

Video	SR = 10%								
	TNN-TV [19]	SNN-TV [17]	t-CTV [3]	TC-NTTNN [21]	GTNN [20]	LRQTC [11]	QT-RNNS1 [32]	NTQTTV1	NTQTTV2
foreman	20.60 / 0.638	22.08 / 0.667	26.94 / 0.738	25.73 / 0.704	25.98 / 0.685	20.89 / 0.588	26.37 / 0.731	**28.53** / **0.755**	27.20 / 0.753
suzie	27.28 / 0.759	25.99 / 0.752	30.89 / 0.783	27.01 / 0.729	28.38 / 0.715	24.80 / 0.700	28.85 / 0.769	**34.19** / **0.805**	32.87 / 0.797
akiyo	25.42 / 0.729	27.49 / 0.760	34.52 / 0.818	35.41 / 0.823	34.20 / 0.801	23.79 / 0.654	36.04 / 0.823	**36.39** / **0.824**	36.14 / **0.824**
container	19.85 / 0.626	22.24 / 0.677	31.69 / 0.805	33.37 / 0.810	**34.87** / 0.808	21.40 / 0.639	34.60 / **0.817**	33.82 / 0.815	33.41 / 0.815
hall	21.01 / 0.699	22.20 / 0.723	31.37 / 0.816	30.15 / 0.812	29.35 / 0.803	21.47 / 0.713	30.92 / 0.814	**32.04** / **0.818**	31.12 / 0.815
grandma	26.10 / 0.756	27.25 / 0.771	33.69 / 0.819	34.00 / 0.820	33.38 / 0.815	25.29 / 0.738	34.49 / 0.823	**35.56** / **0.825**	34.97 / **0.825**
news	20.18 / 0.647	21.13 / 0.677	32.17 / 0.809	31.38 / 0.810	30.68 / 0.776	21.14 / 0.619	32.78 / 0.813	**33.33** / **0.818**	31.29 / 0.813
carphone	23.20 / 0.665	24.76 / 0.705	30.39 / 0.777	29.94 / 0.772	28.83 / 0.723	22.13 / 0.599	29.93 / 0.775	**31.54** / **0.789**	30.54 / 0.785
Video	SR = 5%								
	TNN-TV [19]	SNN-TV [17]	t-CTV [3]	TC-NTTNN [21]	GTNN [20]	LRQTC [11]	QT-RNNS1 [32]	NTQTTV1	NTQTTV2
foreman	19.47 / 0.572	19.70 / 0.577	25.17 / 0.700	23.42 / 0.638	22.22 / 0.571	18.24 / 0.502	24.69 / 0.693	**26.53** / 0.719	25.80 / **0.729**
suzie	24.26 / 0.722	25.33 / 0.737	30.83 / 0.782	28.75 / 0.758	28.75 / 0.728	22.48 / 0.669	30.88 / 0.784	**32.47** / **0.794**	31.41 / 0.786
akiyo	22.29 / 0.648	24.38 / 0.712	30.98 / 0.802	32.18 / 0.812	28.47 / 0.721	21.37 / 0.593	33.17 / 0.815	**34.12** / **0.818**	33.70 / 0.815
container	18.55 / 0.560	20.13 / 0.605	27.17 / 0.770	29.48 / 0.790	26.62 / 0.729	19.46 / 0.574	30.62 / 0.799	**30.91** / **0.800**	30.41 / **0.800**
hall	19.06 / 0.650	19.73 / 0.663	27.76 / 0.798	27.79 / 0.800	24.96 / 0.761	19.11 / 0.662	28.70 / 0.805	**30.00** / **0.810**	29.09 / 0.807
grandma	23.65 / 0.714	24.42 / 0.735	31.04 / 0.804	31.49 / 0.810	29.74 / 0.788	23.03 / 0.692	32.35 / 0.816	**33.56** / **0.819**	33.07 / **0.819**
news	18.56 / 0.571	19.32 / 0.611	27.56 / 0.774	28.25 / 0.789	24.11 / 0.652	18.44 / 0.516	30.13 / 0.797	31.20 / 0.807	28.78 / 0.799
carphone	20.46 / 0.569	21.42 / 0.615	28.05 / 0.748	27.10 / 0.731	24.38 / 0.614	19.35 / 0.530	27.88 / 0.749	**29.70** / **0.768**	28.70 / 0.762
Video	SR = 3%								
	TNN-TV [19]	SNN-TV [17]	t-CTV [3]	TC-NTTNN [21]	GTNN [20]	LRQTC [11]	QT-RNNS1 [32]	NTQTTV1	NTQTTV2
foreman	18.78 / 0.524	18.48 / 0.522	23.53 / 0.662	21.70 / 0.580	19.47 / 0.479	15.95 / 0.433	23.05 / 0.653	**24.86** / 0.680	24.53 / **0.704**
suzie	22.33 / 0.699	23.43 / 0.715	29.49 / 0.770	26.82 / 0.729	25.41 / 0.672	20.53 / 0.649	29.40 / 0.771	**31.29** / **0.785**	31.15 / 0.783
akiyo	19.51 / 0.570	22.15 / 0.670	28.56 / 0.776	30.05 / 0.799	24.10 / 0.622	18.36 / 0.527	31.40 / 0.805	**32.26** / **0.810**	31.84 / 0.804
container	17.68 / 0.501	18.87 / 0.555	24.40 / 0.727	26.91 / 0.768	21.40 / 0.599	18.82 / 0.557	27.79 / 0.777	27.67 / 0.771	**28.24** / **0.783**
hall	17.92 / 0.626	18.63 / 0.635	25.07 / 0.774	25.97 / 0.787	20.91 / 0.692	17.97 / 0.635	26.62 / 0.792	**27.57** / 0.795	27.44 / **0.797**
grandma	22.17 / 0.669	23.14 / 0.711	29.14 / 0.788	29.71 / 0.799	26.52 / 0.754	21.46 / 0.669	31.02 / 0.809	**32.04** / 0.811	31.82 / **0.813**
news	17.15 / 0.498	18.41 / 0.566	24.22 / 0.727	25.73 / 0.763	20.43 / 0.540	15.96 / 0.431	27.70 / 0.774	**28.45** / **0.788**	26.85 / 0.782
carphone	18.55 / 0.499	19.89 / 0.564	26.19 / 0.712	25.31 / 0.694	21.39 / 0.523	16.75 / 0.428	26.34 / 0.724	**28.25** / **0.744**	27.39 / 0.741
Time (s)	530.77	191.03	710.28	62.22	64.49	80.75	1787.66	2191.50	1288.04

structures. Let $\gamma = |\Gamma|$ denote the cardinality of this set. Then, the nonlinear quaternion tensor total variation norm of $\dot{\mathcal{X}}$ is defined as

$$\|\dot{\mathcal{X}}\|_{\text{NTQTTV1}} := \frac{1}{\gamma}\sum_{d\in\Gamma}\|\nabla_d(\psi(\dot{\mathcal{X}}))\|_{\text{QTNN}}. \tag{4}$$

Although NTQTTV1 computes directional gradients along each mode separately to model low-rankness and smoothness, this design can become computationally expensive for high-order tensors in optimization. To address this issue while retaining modeling effectiveness, we propose the second

TABLE IV

PERFORMANCE (PSNR/ASSIM VALUES) OF DIFFERENT RECOVERY ALGORITHMS FOR 8 LIGHT FIELD IMAGES. THE BEST NUMERICAL RESULTS ARE HIGHLIGHTED IN BOLD, AND THE SECOND-BEST RESULTS ARE UNDERLINED

Light Field	SR = 1%								
Image	TNN-TV [19]	SNN-TV [17]	t-CTV [3]	TC-NTTNN [21]	GTNN [20]	LRQTC [11]	QT-RNNS1 [32]	NTQTTV1	NTQTTV2
bedroom	21.11 / 0.665	15.61 / 0.538	29.06 / 0.823	25.81 / 0.670	14.81 / 0.247	9.06 / 0.072	27.94 / 0.819	27.25 / 0.714	**29.26 / 0.851**
books	17.61 / 0.746	12.90 / 0.568	23.09 / 0.814	20.60 / 0.721	12.58 / 0.409	7.59 / 0.031	18.80 / 0.760	**23.53 / 0.856**	23.32 / 0.842
herbs	18.75 / 0.737	12.42 / 0.543	22.96 / 0.798	20.95 / 0.688	12.51 / 0.389	6.74 / 0.037	18.78 / 0.744	22.83 / 0.819	**24.24 / 0.853**
origami	14.68 / 0.649	9.88 / 0.409	14.37 / 0.629	15.04 / 0.655	10.26 / 0.411	4.96 / 0.013	13.40 / 0.654	**21.04 / 0.900**	19.93 / 0.873
box	21.00 / 0.531	16.04 / 0.325	24.28 / 0.672	20.94 / 0.433	16.88 / 0.323	11.44 / 0.005	21.29 / 0.495	24.55 / 0.902	**27.76 / 0.958**
boardgames	23.05 / 0.877	17.00 / 0.692	27.02 / 0.885	24.67 / 0.858	16.48 / 0.594	9.63 / 0.003	26.35 / 0.902	26.70 / 0.909	**28.09 / 0.920**
dino	18.65 / 0.781	12.66 / 0.550	25.70 / 0.847	22.30 / 0.738	12.68 / 0.347	7.06 / 0.036	19.91 / 0.781	24.27 / 0.839	**26.92 / 0.897**
sideboard	16.20 / 0.611	11.22 / 0.430	19.07 / 0.674	16.70 / 0.531	11.47 / 0.351	6.27 / 0.018	14.91 / 0.559	19.17 / 0.671	**19.64 / 0.695**
Light Field	SR = 0.7%								
Image	TNN-TV [19]	SNN-TV [17]	t-CTV [3]	TC-NTTNN [21]	GTNN [20]	LRQTC [11]	QT-RNNS1 [32]	NTQTTV1	NTQTTV2
bedroom	19.23 / 0.608	11.62 / 0.336	27.69 / 0.785	24.68 / 0.631	12.18 / 0.167	8.41 / 0.003	21.01 / 0.683	25.88 / 0.702	**28.41 / 0.836**
books	15.58 / 0.698	9.86 / 0.305	21.92 / 0.740	20.04 / 0.707	10.44 / 0.260	7.23 / 0.008	15.67 / 0.674	**22.88 / 0.834**	22.77 / 0.830
herbs	16.18 / 0.692	9.03 / 0.304	21.65 / 0.723	20.45 / 0.673	9.86 / 0.236	6.33 / 0.009	14.63 / 0.625	22.35 / 0.801	**23.66 / 0.838**
origami	13.27 / 0.586	7.07 / 0.193	14.09 / 0.539	14.64 / 0.630	7.95 / 0.235	4.70 / 0.004	10.83 / 0.497	**20.49 / 0.891**	19.21 / 0.851
box	19.04 / 0.905	7.42 / 0.368	24.66 / 0.855	25.80 / 0.936	8.07 / 0.307	3.78 / 0.004	12.00 / 0.720	24.16 / 0.904	**27.23 / 0.955**
boardgames	21.23 / 0.844	12.89 / 0.340	25.01 / 0.799	24.09 / 0.848	13.59 / 0.367	9.62 / 0.002	22.61 / 0.858	26.38 / 0.897	**27.62 / 0.914**
dino	16.23 / 0.717	9.43 / 0.294	24.39 / 0.776	21.39 / 0.718	10.15 / 0.205	6.58 / 0.002	15.46 / 0.657	23.66 / 0.826	**26.05 / 0.885**
sideboard	14.24 / 0.560	8.43 / 0.226	18.12 / 0.589	16.41 / 0.525	9.26 / 0.215	5.98 / 0.006	12.54 / 0.470	18.82 / 0.652	**19.23 / 0.678**
Light Field	SR = 0.5%								
Image	TNN-TV [19]	SNN-TV [17]	t-CTV [3]	TC-NTTNN [21]	GTNN [20]	LRQTC [11]	QT-RNNS1 [32]	NTQTTV1	NTQTTV2
bedroom	15.77 / 0.534	9.78 / 0.167	26.63 / 0.728	23.69 / 0.599	10.74 / 0.121	8.40 / 0.002	16.69 / 0.566	25.49 / 0.706	**27.62 / 0.819**
books	13.06 / 0.600	8.22 / 0.103	20.36 / 0.633	19.48 / 0.695	9.16 / 0.160	7.09 / 0.001	13.22 / 0.559	**22.52** / 0.816	22.20 / **0.818**
herbs	12.99 / 0.587	7.41 / 0.122	20.24 / 0.622	19.96 / 0.651	8.49 / 0.143	6.18 / 0.001	12.13 / 0.509	22.31 / 0.795	**23.17 / 0.826**
origami	10.69 / 0.461	5.61 / 0.058	13.74 / 0.440	14.27 / 0.608	6.70 / 0.128	4.58 / 0.001	9.20 / 0.366	**19.82 / 0.879**	18.72 / 0.831
box	12.72 / 0.777	5.22 / 0.113	21.15 / 0.718	24.87 / 0.930	6.29 / 0.167	3.69 / 0.002	9.41 / 0.556	24.84 / 0.917	**26.71 / 0.952**
boardgames	17.26 / 0.712	11.01 / 0.118	23.49 / 0.684	23.44 / 0.840	12.05 / 0.213	9.61 / 0.002	18.54 / 0.758	25.52 / 0.889	**27.13 / 0.909**
dino	13.24 / 0.609	7.80 / 0.120	22.34 / 0.674	20.88 / 0.709	8.80 / 0.131	6.57 / 0.001	12.82 / 0.537	23.98 / 0.822	**25.09 / 0.871**
sideboard	11.75 / 0.463	6.93 / 0.077	16.92 / 0.491	16.23 / 0.522	7.99 / 0.127	5.85 / 0.001	10.84 / 0.384	18.39 / 0.633	**18.88 / 0.664**

nonlinear transformed quaternion tensor total variation norm (NTQTTV2), which is more computationally efficient.

Please note that our proposed NTQTTV2 norm is structurally different from the traditional Total Variation (TV) norm (which is defined as a sum of variations). We define it as a "product norm" as it is more computationally efficient (see our complexity analysis in Section III-C), while still serving as an effective regularizer. We retain the NTQTTV2 name to reflect its conceptual link to the TV framework.

Definition 6 (NTQTTV2): For $\dot{\mathcal{X}} \in \mathbb{H}^{n_1 \times \cdots \times n_k}$, we first define the sequential product operation used to achieve our computational gain. This operation is computed by:

$$\psi(\dot{\mathcal{X}}) \times_{i=1}^{k} \mathbf{D}_{n_i} := \psi(\dot{\mathcal{X}}) \times_1 \mathbf{D}_{n_1} \times_2 \mathbf{D}_{n_2} \cdots \times_k \mathbf{D}_{n_k}, \quad (5)$$

where $\mathbf{D}_{n_i}$ is a row circulant matrix of $(-w_{n_i}, w_{n_i}, 0, \ldots, 0)$, and $w_{n_i} \in \mathbb{R}^+$. Notably, the multiplication order of the modules is commutative.

The second nonlinear transformed quaternion tensor total variation (NTQTTV2) norm of $\dot{\mathcal{X}}$ is then defined as the QTNN norm of this product:

$$\|\dot{\mathcal{X}}\|_{\text{NTQTTV2}} := \|\psi(\dot{\mathcal{X}}) \times_{i=1}^{k} \mathbf{D}_{n_i}\|_{\text{QTNN}}. \quad (6)$$

After defining the nonlinear transformed low-rank quaternion tensor total variation regularizers, our multidimensional color completion model is formulated as

$$\min_{\dot{\mathcal{X}}} \|\dot{\mathcal{X}}\|_{\text{NTQTTV}} \quad \text{s.t. } P_\Omega(\dot{\mathcal{X}}) = P_\Omega(\dot{\mathcal{O}}), \quad (7)$$

where $\mathcal{P}_\Omega(\cdot)$ is the projection function that keeps the elements in the observed set Ω and makes others zero, and $\|\cdot\|_{\text{NTQTTV}}$ can be NTQTTV1 or NTQTTV2 for conciseness. By using these regularizers, we can simultaneously exploit the global low-rankness, local smoothness, and nonlinearity of the multidimensional color images, with the intrinsic color correlations well preserved. It is noteworthy that this modeling strategy is not limited to the QTNN deduced within the TQt-SVD framework, as it can be flexibly extended to other quaternion tensor decomposition schemes, offering a general paradigm for integrating structural priors and nonlinear characteristics in multidimensional color image processing.

The proposed model in (7) maintains profound connections to previous methods. Under specific conditions, the proposed NTQTTV model can be simplified to existing norm formulations: (1) without differencing, it reduces to the nonlinear transform-based quaternion tensor nuclear norm (QTNN); (2) without the nonlinear function, it degenerates to the correlated total variation that jointly models low-rankness and smoothness in the quaternion domain; (3) when the field is real-valued, it can be viewed as a combination of nonlinear transform methods for real-valued tensors [3] and tensor correlated total variation [21].

B. Proposed Algorithms

In this part, we tailor the alternating direction method of multipliers (ADMM) [31] algorithms to solve the proposed

NTQTTV1 regularized models. As the space is limited, the detailed algorithm for NTQTTV2 is in the Supplementary Material. After introducing auxiliary variables, (7) can be equivalently reformulated as

$$\begin{aligned}&\min_{\dot{\mathcal{N}}_d,\dot{\mathcal{X}}} \frac{1}{\gamma}\sum_{d\in\Gamma}\|\dot{\mathcal{N}}_d\|_{\text{QTNN}}\\&\text{s.t. } \dot{\mathcal{N}}_d=\nabla_d(\dot{\mathcal{Z}}),\dot{\mathcal{Z}}=\psi(\dot{\mathcal{X}}),\ P_\Omega(\dot{\mathcal{X}})=P_\Omega(\dot{\mathcal{O}}).\end{aligned}\tag{8}$$

Then, the augmented Lagrangian function is formulated as follows.

$$\begin{aligned}&L(\dot{\mathcal{N}}_d,\dot{\mathcal{Z}},\dot{\mathcal{W}},\dot{\mathcal{X}},\dot{\mathcal{P}}_d,\dot{\mathcal{Q}},\dot{\Lambda})\\&=\sum_{d\in\Gamma}(\frac{1}{\gamma}\|\dot{\mathcal{N}}_d\|_{\text{QTNN}}+\frac{\beta}{2}\|\dot{\mathcal{N}}_d-\nabla_d(\dot{\mathcal{Z}})\|_F^2\\&\quad+\Re(\langle\dot{\mathcal{P}}_d,\dot{\mathcal{N}}_d-\nabla_d(\dot{\mathcal{Z}})\rangle))+\frac{\beta}{2}\|\dot{\mathcal{Z}}-\psi(\dot{\mathcal{W}})\|_F^2\\&\quad+\Re(\langle\dot{\mathcal{Q}},\dot{\mathcal{Z}}-\psi(\dot{\mathcal{W}})\rangle)+\frac{\beta}{2}\|\dot{\mathcal{W}}-\dot{\mathcal{X}}\|_F^2\\&\quad+\Re(\langle\dot{\Lambda},\dot{\mathcal{W}}-\dot{\mathcal{X}}\rangle)+\mathcal{I}_\Omega(\dot{\mathcal{X}}),\end{aligned}\tag{9}$$

where $\dot{\mathcal{P}}_d$, $\dot{\mathcal{Q}}$, and $\dot{\Lambda}$ are the Lagrange multipliers, $\mathcal{I}_\Omega(\cdot)$ is the indicator function satisfies $\mathcal{I}_\Omega(\dot{\mathcal{X}})=0$ if $\dot{\mathcal{X}}\in\Omega$ and ∞ otherwise, and β is the positive penalty parameter. Under the framework of ADMM, the variables are updated alternately in the $(j+1)$-th iteration using

$$\begin{cases}\dot{\mathcal{N}}_d^{j+1}=\arg\min_{\dot{\mathcal{N}}_d} L(\dot{\mathcal{N}}_d^{j},\dot{\mathcal{Z}}^{j},\dot{\mathcal{W}}^{j},\dot{\mathcal{X}}^{j},\dot{\mathcal{P}}_d^{j},\dot{\mathcal{Q}}^{j},\dot{\Lambda}^{j},\beta^{j}),\\ \dot{\mathcal{Z}}^{j+1}=\arg\min_{\dot{\mathcal{Z}}} L(\dot{\mathcal{N}}_d^{j+1},\dot{\mathcal{Z}}^{j},\dot{\mathcal{W}}^{j},\dot{\mathcal{X}}^{j},\dot{\mathcal{P}}_d^{j},\dot{\mathcal{Q}}^{j},\dot{\Lambda}^{j},\beta^{j}),\\ \dot{\mathcal{W}}^{j+1}=\arg\min_{\dot{\mathcal{W}}} L(\dot{\mathcal{N}}_d^{j+1},\dot{\mathcal{Z}}^{j+1},\dot{\mathcal{W}}^{j},\dot{\mathcal{X}}^{j},\dot{\mathcal{P}}_d^{j},\dot{\mathcal{Q}}^{j},\dot{\Lambda}^{j},\beta^{j}),\\ \dot{\mathcal{X}}^{j+1}=\arg\min_{\dot{\mathcal{X}}} L(\dot{\mathcal{N}}_d^{j+1},\dot{\mathcal{Z}}^{j+1},\dot{\mathcal{W}}^{j+1},\dot{\mathcal{X}}^{j},\dot{\mathcal{P}}_d^{j},\dot{\mathcal{Q}}^{j},\dot{\Lambda}^{j},\beta^{j}),\\ \dot{\mathcal{P}}_d^{j+1}=\dot{\mathcal{P}}_d^{j}+\beta^{j}(\dot{\mathcal{N}}_d^{j+1}-\nabla_d(\dot{\mathcal{Z}}^{j+1})),\\ \dot{\mathcal{Q}}^{j+1}=\dot{\mathcal{Q}}^{j}+\beta^{j}(\dot{\mathcal{Z}}^{j+1}-\psi(\dot{\mathcal{W}}^{j+1})),\\ \dot{\Lambda}^{j+1}=\dot{\Lambda}^{j}+\beta^{j}(\dot{\mathcal{W}}^{j+1}-\dot{\mathcal{X}}^{j+1}),\\ \beta^{j+1}=\min\{\beta^{j}\eta,\beta_{\max}\}.\end{cases}\tag{10}$$

The $\dot{\mathcal{N}}_d, d\in\Gamma$ subproblem is

$$\begin{aligned}\dot{\mathcal{N}}_d^{j+1}&=\arg\min_{\dot{\mathcal{N}}_d}\frac{1}{\gamma}\|\dot{\mathcal{N}}_d\|_{\text{QTNN}}+\frac{\beta^j}{2}\|\dot{\mathcal{N}}_d-\nabla_d(\dot{\mathcal{Z}}^j)\|_F^2\\&\quad+\Re(\langle\dot{\mathcal{P}}_d^j,\dot{\mathcal{N}}_d-\nabla_d(\dot{\mathcal{Z}}^j)\rangle)\\&=\arg\min_{\dot{\mathcal{N}}_d}\frac{1}{\gamma}\|\dot{\mathcal{N}}_d\|_{\text{QTNN}}+\frac{\beta^j}{2}\|\dot{\mathcal{N}}_d-\nabla_d(\dot{\mathcal{Z}}^j)+\frac{\dot{\mathcal{P}}_d^j}{\beta}\|_F^2.\end{aligned}\tag{11}$$

This problem can be solved by the quaternion tensor singular value thresholding (QTSVT) we proposed in [32].

Definition 7 (QTSVT [32]): Let $\dot{\mathcal{X}}=\dot{\mathcal{U}}\star_{QT}\dot{\mathcal{D}}\star_{QT}\dot{\mathcal{V}}^H$ be the QTt-SVD of $\dot{\mathcal{X}}$. For any $\tau>0$, the QTSVT operator is defined as

$$\mathfrak{D}_\tau(\dot{\mathcal{X}})=\dot{\mathcal{U}}\star_{QT}\dot{\mathcal{D}}_\tau\star_{QT}\dot{\mathcal{V}}^H,\tag{12}$$

where $\dot{\mathcal{D}}_\tau=\mathcal{L}^{-1}((\mathcal{L}(\dot{\mathcal{D}})-\tau)_+)$.

Theorem 2: Let $\mathcal{L}$ be the linear transform which is utilized in TQt-SVD, for any $\tau>0$ and $\dot{\mathcal{X}}\in\mathbb{H}^{n_1\times n_2\times\cdots\times n_k}$, the QTSVT in (12) obeys

$$\mathfrak{D}_\tau(\dot{\mathcal{X}})=\arg\min_{\dot{\mathcal{T}}}\tau\|\dot{\mathcal{T}}\|_{\text{QTNN}}+\frac{1}{2}\|\dot{\mathcal{T}}-\dot{\mathcal{X}}\|_F^2.\tag{13}$$

Hence, (11) can be solved by

$$\hat{\dot{\mathcal{N}}}_d^{j+1}=\mathfrak{D}_{\frac{1}{\beta^j\gamma}}\left(\nabla_d(\dot{\mathcal{Z}}^j)-\frac{\dot{\mathcal{P}}_d^j}{\beta}\right).\tag{14}$$

The $\dot{\mathcal{Z}}$ subproblem is

$$\begin{aligned}\dot{\mathcal{Z}}^{j+1}&=\arg\min_{\dot{\mathcal{Z}}}\frac{\beta^j}{2}\sum_{d\in\Gamma}\|\nabla_d(\dot{\mathcal{Z}})-\dot{\mathcal{N}}_d^{j+1}-\frac{\dot{\mathcal{P}}_d^j}{\beta^j}\|_F^2\\&\quad+\frac{\beta^j}{2}\|\dot{\mathcal{Z}}-\psi(\dot{\mathcal{W}}^j)+\frac{\dot{\mathcal{Q}}^j}{\beta^j}\|_F^2.\end{aligned}\tag{15}$$

Following the quaternion-based derivation proposed in [33], the left derivative of equation (15) with respect to $\dot{\mathcal{Z}}$ leads to the following linear equation.

$$\sum_{d\in\Gamma}\nabla_d^T\left(\nabla_d(\dot{\mathcal{Z}})-\dot{\mathcal{N}}_d-\frac{\dot{\mathcal{P}}_d^j}{\beta^j}\right)+\dot{\mathcal{Z}}-\psi(\dot{\mathcal{W}}^j)+\frac{\dot{\mathcal{Q}}^j}{\beta^j}=0.\tag{16}$$

In the above model, the linear system for updating the quaternion tensor $\dot{\mathcal{Z}}$ involves multiple difference operators along spatial and color dimensions. Although applied to quaternion-valued data, these operators are constructed from real-valued circulant matrices and thus preserve linearity under the quaternion tensor-tensor product. Due to their real structure and the convolution theorem in the real domain, these difference tensors can be efficiently diagonalized using the Fast Fourier Transform (FFT) [34]. Specifically, the convolution with real-valued difference kernels becomes element-wise multiplication in the frequency domain, allowing terms like $\nabla_k^\top\nabla_k$ to be expressed as component-wise multiplication of power spectra, i.e., $\mathcal{F}(\mathcal{D}_k)^*\circ\mathcal{F}(\mathcal{D}_k)$, where $\circ$ denotes component-wise multiplication. Furthermore, FFT in the quaternion domain also satisfies Parseval's identity [35], ensuring energy preservation across domains. This framework enables efficient and stable computation, leading to a closed-form frequency-domain solution for quaternion tensor optimization as follows.

$$\dot{\mathcal{Z}}^{j+1}=\mathcal{Q}\mathcal{F}^{-1}\left(\frac{\mathcal{Q}\mathcal{F}\left(\psi(\dot{\mathcal{W}}^j)-\frac{\dot{\mathcal{Q}}^j}{\beta^j}+\dot{\mathcal{S}}^j\right)}{\mathbf{1}+\sum_{d\in\Gamma}\mathcal{F}(\mathcal{D}_d)^*\circ\mathcal{F}(\mathcal{D}_d)}\right),\tag{17}$$

where $\dot{\mathcal{S}}^j=\sum_{d\in\Gamma}\mathcal{F}(\mathcal{D}_k)^*\circ\mathcal{Q}\mathcal{F}\left(\dot{\mathcal{N}}_d^{j+1}+\frac{\dot{\mathcal{P}}_d^j}{\beta^j}\right)$, and $\mathbf{1}$ is a tensor with all entries equal to one.

The $\dot{\mathcal{W}}$ subproblem is

$$\begin{aligned}\dot{\mathcal{W}}^{j+1}&=\arg\min_{\dot{\mathcal{W}}}\frac{\beta^j}{2}\|\psi(\dot{\mathcal{W}})-\dot{\mathcal{Z}}^{j+1}-\frac{\dot{\mathcal{Q}}^j}{\beta}\|_F^2\\&\quad+\frac{\beta}{2}\|\dot{\mathcal{W}}-\dot{\mathcal{X}}^j+\frac{\dot{\Lambda}^j}{\beta^j}\|_F^2.\end{aligned}\tag{18}$$

Due to the inclusion of the nonlinear function in (18), it is challenging to solve $\|\psi(\dot{\mathcal{W}})-\dot{\mathcal{Z}}^{j+1}-\frac{\dot{\mathcal{Q}}^j}{\beta^j}\|_F^2$ directly. Motivated by the local linear approximation for solving the nonlinear activation function in the Frobenius norm proposed in [36], this paper develops a first-order approximation of $F_\psi(\dot{\mathcal{W}};\dot{\mathcal{H}})=\|\psi(\dot{\mathcal{W}})-\dot{\mathcal{H}}\|_F^2$. Based on the theory of quaternion matrix derivatives presented in [33] and the Taylor's theorem of the left kind introduced in [37], the first-order approximation of the original function $F_\psi(\dot{\mathcal{W}};\dot{\mathcal{H}})$ is computed at the time of the

latest update, rather than updating the variables themselves. This can be expressed as

$$\begin{aligned}
&F_{\psi}^{j}(\dot{\mathcal{W}};\dot{\mathcal{H}})\\
&:= F_{\psi}(\dot{\mathcal{W}}^{j-1};\dot{\mathcal{H}}) + 4\Re\left(\frac{\partial F_{\psi}(\dot{\mathcal{W}}^{j-1};\dot{\mathcal{H}})}{\partial \dot{\mathcal{W}}^{*}}(\dot{\mathcal{W}}-\dot{\mathcal{W}}^{j-1})^{*}\right)\\
&\quad + 2\,h^{j}\sum_{v\in\{1,i,j,k\}}\Re\left((\dot{\mathcal{W}}-\dot{\mathcal{W}}^{j-1})_{v}^{*}(\dot{\mathcal{W}}-\dot{\mathcal{W}}^{j-1})^{*}\right)\\
&= F_{\psi}(\dot{\mathcal{W}}^{j-1};\dot{\mathcal{H}}) + 4\Re\left(\frac{\partial F_{\psi}(\dot{\mathcal{W}}^{j-1};\dot{\mathcal{H}})}{\partial \dot{\mathcal{W}}^{*}}(\dot{\mathcal{W}}-\dot{\mathcal{W}}^{j-1})^{*}\right)\\
&\quad + 2\,h^{j}\|\dot{\mathcal{W}}-\dot{\mathcal{W}}^{j-1}\|_{F}^{2}, \qquad (19)
\end{aligned}$$

where $\dot{\mathcal{W}}^{j-1}$ is the $(j-1)$-th iteration, h is specified as the upper bounds of the locally Lipschitz constants of functions $F_{\psi}^{j}(\dot{\mathcal{W}};\dot{\mathcal{H}})$, shown as $h=\hat{\mathcal{L}}(\|\dot{\mathcal{H}}\|_{\max})$.

Let $\psi(\dot{\mathcal{W}})-\dot{\mathcal{H}} = (\phi(\mathcal{W}_0)-\mathcal{H}_0)+\mathbf{i}(\phi(\mathcal{W}_1)-\mathcal{H}_1)+\mathbf{j}(\phi(\mathcal{W}_2)-\mathcal{H}_2)+\mathbf{k}(\phi(\mathcal{W}_3)-\mathcal{H}_3)$, based on the chain rules proposed in the quaternion domain, it follows that

$$\begin{aligned}
&\frac{\partial F_{\psi}(\dot{\mathcal{W}};\dot{\mathcal{H}})}{\partial \dot{\mathcal{W}}^{*}}\\
&= 2(\phi(\mathcal{W}_0)-\mathcal{H}_0)\left(\frac{\partial\phi(\mathcal{W}_0)}{\partial \mathcal{W}_0^{*}}\right) + 2(\phi(\mathcal{W}_1)-\mathcal{H}_1)\left(\frac{\partial\phi(\mathcal{W}_1)}{\partial \mathcal{W}_1^{*}}\right)\\
&\quad +2(\phi(\mathcal{W}_2)-\mathcal{H}_2)\left(\frac{\partial\phi(\mathcal{W}_2)}{\partial \mathcal{W}_2^{*}}\right) + 2(\phi(\mathcal{W}_3)-\mathcal{H}_3)\left(\frac{\partial\phi(\mathcal{W}_3)}{\partial \mathcal{W}_3^{*}}\right),
\end{aligned}$$

where $\psi(\cdot)$ is a nonlinear split-quaternion function $\psi(\dot{\mathcal{W}}) = \phi(\mathcal{W}_0)+\mathbf{i}\phi(\mathcal{W}_1)+\mathbf{j}\phi(\mathcal{W}_2)+\mathbf{k}\phi(\mathcal{W}_3)$, and $\phi(\cdot)$ is a real-valued differentiable function. Then,

$$\frac{\partial\phi(\mathcal{W}_0)}{\partial \mathcal{W}_0^{*}} = \frac{1}{4}\phi'(\mathcal{W}_0).$$

In a similar way, $\frac{\partial\phi(\mathcal{W}_1)}{\partial \mathcal{W}_1^{*}} = \frac{i}{4}\phi'(\mathcal{W}_1)$, $\frac{\partial\phi(\mathcal{W}_2)}{\partial \mathcal{W}_2^{*}} = \frac{j}{4}\phi'(\mathcal{W}_2)$, $\frac{\partial\phi(\mathcal{W}_3)}{\partial \mathcal{W}_3^{*}} = \frac{k}{4}\phi'(\mathcal{W}_3)$. Further, based on the product rule in the quaternion domain, it follows that

$$\begin{aligned}
&\sum_{v\in\{1,i,j,k\}}\Re\left(\frac{\partial^{2}F_{\psi}(\dot{\mathcal{W}};\dot{\mathcal{H}})}{\partial \dot{\mathcal{W}}_{v}^{*}\partial \dot{\mathcal{W}}^{*}}\right)\\
&= \frac{1}{8}((\phi'(\mathcal{W}_0))^{2}+(\phi(\mathcal{W}_0)-\mathcal{H}_0)\phi''(\mathcal{W}_0))\\
&\quad +(\phi'(\mathcal{W}_1)^{2}+(\phi(\mathcal{W}_1)-\mathcal{H}_1)\phi''(\mathcal{W}_1))\\
&\quad +(\phi'(\mathcal{W}_2)^{2}+(\phi(\mathcal{W}_2)-\mathcal{H}_2)\phi''(\mathcal{W}_2))\\
&\quad +(\phi'(\mathcal{W}_3)^{2}+(\phi(\mathcal{W}_3)-\mathcal{H}_3)\phi''(\mathcal{W}_3)).
\end{aligned}$$

Hence,

$$\hat{\mathcal{L}}(|\dot{q}|) := \frac{1}{2}L_2(L_0+|\dot{q}|)+\frac{1}{2}L_1^{2} \qquad (20)$$

is an upper bound of the Lipschitz constant of the gradient of function $(\psi(\dot{u})-\dot{q})^{2}$ with constants. For tanh activation $\phi(u)=\frac{e^{x}-e^{-x}}{e^{x}+e^{-x}}$, $L_0=1, L_1=1$, and $L_2=1$. Based on the prox-linear scheme proposed in [38] to update the subproblems in (18) and the above discuss, the original update of $\dot{\mathcal{W}}^{j+1}$ can be reformulated as

$$\dot{\mathcal{W}}^{j+1} = \arg\min_{\dot{\mathcal{W}}}\left\{F_{\psi}(\dot{\mathcal{W}};\dot{\mathcal{H}}^{j+1})+\|\dot{\mathcal{W}}^{*}-\dot{\Lambda}^{j*}\|_{F}^{2}\right\}, \qquad (21)$$

Algorithm 1 ADMM Solver for Problem (9)

Input: $\dot{\mathcal{O}}$, Ω, tolerance ε, max iterations $J_{\max}$, and parameter β.

Initial $\dot{\mathcal{N}}^{1}=\dot{\mathcal{O}}$, $\dot{\mathcal{W}}^{1}=\dot{\mathcal{O}}$ and $j=1$.
while $j<J_{\max}$ and $\|\dot{\mathcal{X}}^{j+1}-\dot{\mathcal{X}}^{j}\|_{F}\le\varepsilon$ **do**
  Update $\dot{\mathcal{N}}_{d}^{j+1}$ by (14).
  Update $\dot{\mathcal{Z}}^{j+1}$ by (17).
  Update $\dot{\mathcal{W}}^{j+1}$ by (22).
  Update $\dot{\mathcal{X}}^{j+1}$ by (24).
  $\dot{\mathcal{P}}_{d}^{j+1}\leftarrow\dot{\mathcal{P}}_{d}^{j}+\beta^{j}(\dot{\mathcal{N}}_{d}^{j+1}-\nabla_{d}(\dot{\mathcal{Z}}^{j+1}))$.
  $\dot{\mathcal{Q}}^{j+1}\leftarrow\dot{\mathcal{Q}}^{j}+\beta^{j}(\dot{\mathcal{Z}}^{j+1}-\psi(\dot{\mathcal{W}}^{j+1}))$.
  $\dot{\Lambda}^{j+1}\leftarrow\dot{\Lambda}^{j}+\beta^{j}(\dot{\mathcal{W}}^{j+1}-\dot{\mathcal{X}}^{j+1})$.
  $\beta^{j+1}\leftarrow\min\{\beta^{j}\eta,\beta_{\max}\}$.
  $j\leftarrow j+1$.
end while

Output: The recovered quaternion tensor $\dot{\mathcal{X}}_{opt}=\dot{\mathcal{X}}^{j+1}$.

where $\dot{\mathcal{H}}^{j+1}=\dot{\mathcal{Z}}^{j+1}+\frac{\dot{\mathcal{Q}}^{j}}{\beta^{j}}$ and $\dot{\Lambda}^{j}=\dot{\mathcal{X}}^{j}-\frac{\dot{\Lambda}^{j}}{\beta^{j}}$. Let the first derivative of (21) with respect to $\dot{\mathcal{W}}$ be zero, then we have

$$0=\frac{1}{2}(\dot{\mathcal{W}}-\dot{\Lambda}^{j})+\frac{\partial F_{\psi}(\dot{\mathcal{W}}^{j};\dot{\mathcal{H}}^{j+1})}{\partial\dot{\mathcal{W}}}+h(\dot{\mathcal{W}}-\dot{\mathcal{W}}^{j}).$$

Then,

$$\dot{\mathcal{W}}^{j+1}=\left(\dot{\Lambda}^{j}-2\frac{\partial F_{\psi}(\dot{\mathcal{W}}^{j};\dot{\mathcal{H}}^{j+1})}{\partial\dot{\mathcal{W}}}+2h\dot{\mathcal{W}}^{j}\right)/(1+2h). \qquad (22)$$

The $\dot{\mathcal{X}}$ subproblem is

$$\begin{aligned}
\dot{\mathcal{X}}^{j+1} &= \arg\min_{\dot{\mathcal{X}}}\frac{\beta}{2}\|\dot{\mathcal{W}}^{j+1}-\dot{\mathcal{X}}\|_{F}^{2}+\Re(\langle\dot{\Lambda},\dot{\mathcal{W}}-\dot{\mathcal{X}}\rangle)+\mathcal{I}_{\Omega}(\dot{\mathcal{X}})\\
&= \arg\min_{\dot{\mathcal{X}}}\frac{\beta}{2}\|\dot{\mathcal{W}}^{j+1}-\dot{\mathcal{X}}+\frac{\dot{\Lambda}^{j}}{\beta^{j}}\|_{F}^{2}+\mathcal{I}_{\Omega}(\dot{\mathcal{X}}), \qquad (23)
\end{aligned}$$

Hence, we can obtain

$$\dot{\mathcal{X}}^{j+1}=\dot{\mathcal{W}}^{j+1}+\frac{\dot{\Lambda}^{j}}{\beta^{j}},\quad P_{\Omega}(\dot{\mathcal{X}}^{j+1})=P_{\Omega}(\dot{\mathcal{O}}). \qquad (24)$$

The whole procedure to solve (9) is summarized in Algorithm 1. The specific update process for NTQTTV2 is similar to that of NTQTTV1 and is provided in the Supplementary Material. Meanwhile, we establish the convergence guarantees of the proposed nonconvex ADMM algorithms. The informal theorem is presented below.

Theorem 3: The adjacent variables in the Lagrangian function exhibit a consistent trend in the same direction as the number of iterations increases. Besides, the upper bound for the supergradient of the Lagrangian function is given. Then, the sequence converges to a stationary point of equation (9) and satisfies the first-order optimality conditions.

The formal theorem and detailed derivations are provided in the Supplementary Materials.

C. Computational Complexity Analysis

The per-iteration complexity of our algorithms is dominated by the shared QTSVT step. For an input tensor $\dot{\mathcal{O}}\in\mathbb{H}^{n_1\times\cdots\times n_k}$, this primary computational bottleneck involves a multi-mode linear transform and matrix QSVDs, with a

base complexity defined as: $\mathcal{C}_{\text{QTSVT}} = O(n_1 n_2 (n_3 \cdots n_k)^2 + \min(n_1 n_2^2, n_1^2 n_2) n_3 \cdots n_k)$. The total complexity of each algorithm is this base cost plus the cost of their unique operations.

Let $N = n_1 \cdots n_k$. The total complexity of Algorithm 1 (NTQTTV1) is $\mathcal{C}_{\text{QTSVT}} + O\left(N \sum_{j=1}^{k} n_j + N \log N\right)$. The additional terms arise from the finite difference operator and a QFFT-based computation. The total complexity of Algorithm 2 (NTQTTV2 in the Supplementary Material) is $\mathcal{C}_{\text{QTSVT}} + O\left(N \sum_{j=1}^{k} n_j\right)$. The additional cost stems from the model product operation. When compared to the baseline QTNN minimization algorithm (whose complexity is $\mathcal{C}_{\text{QTSVT}}$), both of our methods introduce necessary computational overhead. A direct comparison shows that Algorithm 1 is more computationally intensive than Algorithm 2 due to the additional $O(N \log N)$ term from its QFFT operation.

This analysis contextualizes the empirical runtimes reported in our experiments and characterizes the scalability of our algorithms: Resolution: Scalability with respect to spatial dimensions (n_1, n_2) is polynomial. The QSVD computation within QTSVT scales approximately cubically, which explains why the runtime gap between our methods and simpler baselines widens for higher-resolution data. Order: Scalability with respect to tensor order (k) is exponential. This is evident from the $(n_3 \cdots n_k)^2$ term within the base complexity $\mathcal{C}_{\text{QTSVT}}$, where adding modes substantially increases the computational cost.

IV. Experimental Results

In this section, the effectiveness of the proposed QTTV method is demonstrated by comparing it with various relevant state-of-the-art methods. Subsection IV-A provides the experimental settings. Subsection IV-B presents the color video recovery results, followed by the 5D light field image recovery results in Subsection IV-C. Finally, the experimental results are discussed in Subsection IV-D.

A. Experimental Settings

1) Compared Methods: TNN-TV [19], SNN-TV [17], t-CTV [3], TC-NTTNN [21], and GTNN [20] are tensor-based methods. LRQTC [11], QT-RNNS1 [32] are quaternion tensor based methods. The differences and relationships among all methods are listed in Table II.

2) Test Data and Experimental Environment: Eight color videos were randomly selected, including *foreman, suzie, akiyo, container, hall, grandma, news, carphone*.[1] In the following experiments, 50 frames are adopted, and eight videos are of size $144 \times 176 \times 3 \times 50$. Due to the lower sampling rate, the preceding and following ten frames of the video were flipped to fully utilize the missing video information, forming a $144 \times 176 \times 3 \times 70$ tensor. The sample rates (SR) are $10\%, 5\%, 3\%$, respectively. Eight color light field images were also randomly selected from the 5D Light Field Dataset[2] as additional test samples. Order-5 light field images are sized $9 \times 9 \times 128 \times 128 \times 3$. The sample rates (SR) are $1\%, 0.7\%, 0.5\%$, respectively. Except for QTTV and t-CTV which can process higher order tensor directly, the light field images are reshaped to 4-D tensors as $81 \times 128 \times 128 \times 3$ for other methods. Besides, the tensor-based methods are applied to RGB channels, respectively. All experiments were implemented in MATLAB R2023b, on a PC with a 3.40GHz CPU and 32GB RAM.

3) Evaluation Index Setting: Two indicators are employed to evaluate the performance of the proposed methods, including peak signal to noise rate (PSNR) and average structural similarity index (aSSIM) along with the third or higher dimensions. The parameters for both NTQTTV1 and NTQTTV2 were configured as follows. For NTQTTV1, the regularization parameters were set to $\beta^1 = 8 \times 10^{-2}$, $\eta = 1.03$, and the convergence tolerance $\epsilon = 10^{-3}$. For NTQTTV2, we set $\beta = 8 \times 10^{-2}$ and $\epsilon = 10^{-3}$.

The parameters $(w_1, w_2, w_3) = (1, 1, 1)$ in the circulant matrices of NTQTTV-1. The parameters (w_1, w_2, w_3) in the circulant matrices of NTQTTV-2 were selected based on the characteristics of the input data. Specifically: For the first two video sequences with large frame-to-frame variations, we set $(w_1, w_2, w_3) = (2, 2, 5)$. For the remaining six videos with relatively smoother temporal dynamics, we used $(w_1, w_2, w_3) = (1, 1, 15)$. For 5D light field images, uniform weights were used: $(w_1, w_2, w_3) = (1, 1, 1)$. Besides, based on the author's codes, the parameters of other compared methods are adjusted to the best.

B. Color Video Recovery

Table III lists the PSNR and aSSIM comparisons for all methods. The optimal numerical results are highlighted in bold, and the second-best results are underlined. As shown, the proposed NTQTTV1 outperforms the alternatives in most cases, with its advantages becoming particularly pronounced at very low SR. The final row reports the average running time, which aligns with our complexity analysis (Section III-C): NTQTTV1 is the most computationally intensive, while NTQTTV2 provides a significant computational advantage over NTQTTV1.

Fig. 3 presents reconstructed frames from color videos at SR = 5%. One frame was randomly selected from each video, and its corresponding PSNR and aSSIM values were computed. The proposed method more effectively restores edges and fine details, as highlighted in the enlarged insets. Fig. 4 shows pixel-value profiles at randomly chosen spatial locations in the reconstructed videos. It is evident that the curves produced by NTQTTV more closely match the original pixel values than those generated by the competing methods.

In comparison with quaternion-based methods, LRQTC is limited due to its reliance on low-rank modeling alone. Although QT-RNNS1 introduces data sparsity, it still utilizes a linear low-rank model. The proposed NTQTTV framework combines nonlinear transformation, low-rank approximation, and smoothness regularization in a unified manner, which results in superior reconstruction performance across various tasks.

[1] Available: http://trace.eas.asu.edu/yuv/

[2] Available: https://lightfield-analysis.uni-konstanz.de/

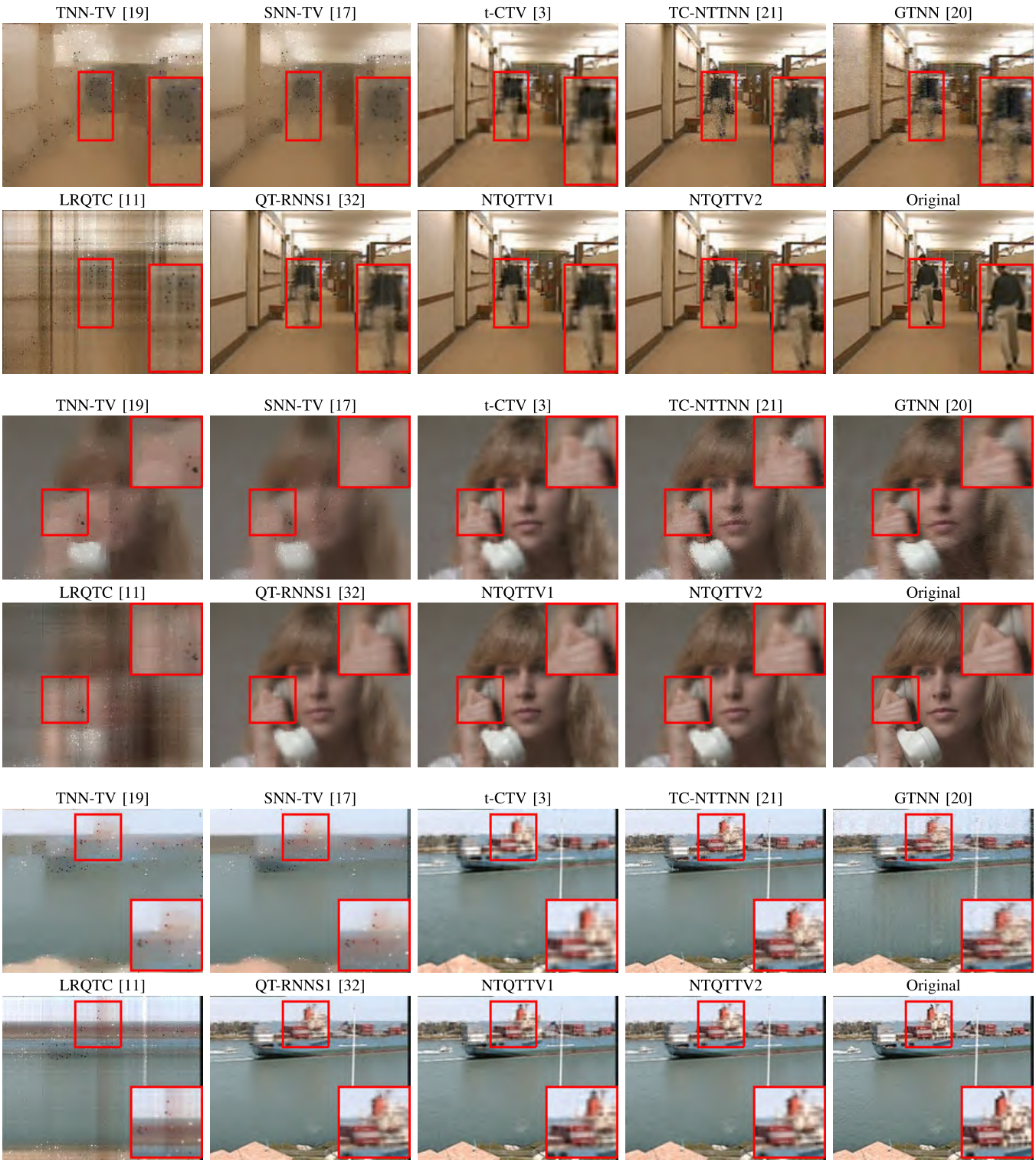

Fig. 3. Restoration results of color videos by different methods respectively with $SR = 5\%$.

C. 5D Light Field Image Recovery

The PSNR and aSSIM metrics for all compared algorithms are presented in Table IV. As shown in Table IV, the proposed NTQTTV2 consistently outperforms the competing methods, with its advantages becoming more pronounced as the SR decreases. Apart from t-CTV, TC-NTTNN, and NTQTTV2, most other approaches fail to reconstruct the light field images. Additionally, all methods demand substantial computational time to address this problem.

The reconstructed visual results of the four top-performing methods (t-CTV, TC-NTTNN, and NTQTTV1 and NTQTTV2) under SR = 0.5% are shown in Fig. 5. Despite the extremely low sampling rate, the proposed method still yields noticeably clearer reconstructions compared to the

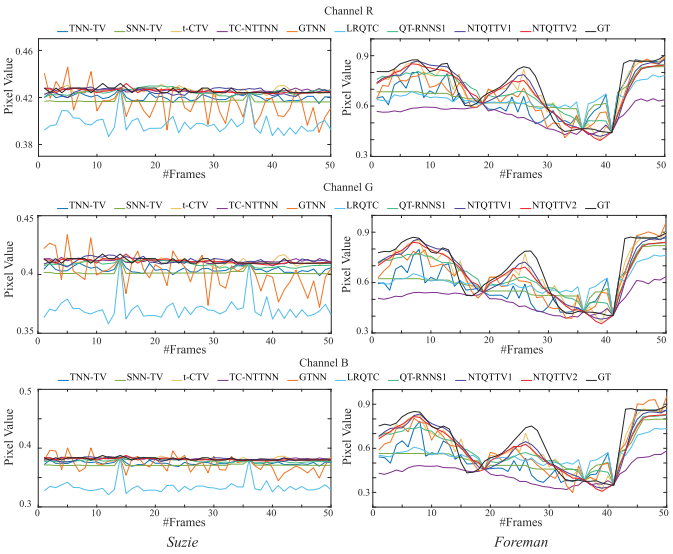

Fig. 4. Comparison of pixel-value profiles at randomly selected spatial locations in the reconstructed *Suzie* and *Foreman* videos ($SR = 5\%$), shown for each of the three color channels.

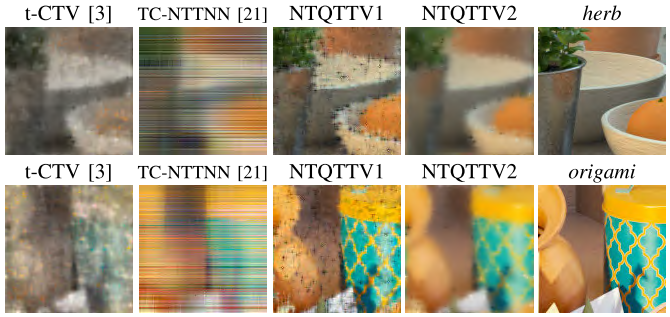

Fig. 5. Restoration result of light field images by different methods with $SR = 0.5\%$.

alternatives. Here, the effectiveness of quaternions in retaining color information can also be visually observed.

The NTQTTV algorithm achieves superior visual and quantitative performance by leveraging quaternion representation, nonlinear transformation, and total variation regularization. These components jointly enhance low-rank approximation and angular detail recovery in light field reconstruction.

While NTQTTV achieves high-quality reconstruction of videos and light field images under challenging missing data conditions, it requires substantial computational resources. Reducing the computational burden is identified as an important direction for future work.

D. Ablation Study and Discussions

1) Convergence Curves of the Proposed NTQTTV Method: This subsection examines the numerical convergence of the NTQTTV method's nonlinear ADMM-based algorithm to verify its theoretical convergence properties. Using the *news* video at different SRs as a test case, Fig. 6 plots the relative change curves of our algorithm. The relative change metric for the quaternion tensor $\dot{\mathcal{X}}$ between consecutive iterations is

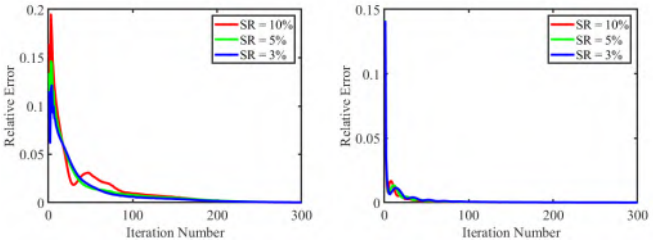

(a) NTQTTV1 (b) NTQTTV2

Fig. 6. Relative error curves of (a) NTQTTV1 and (b) NTQTTV2 under different SRs.

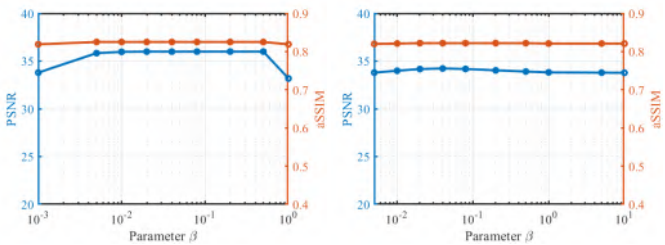

(a) NTQTTV1 (b) NTQTTV2

Fig. 7. PSNR and aSSIM curves of (a) NTQTTV1 and (b) NTQTTV2 under $SR = 0.2$.

defined as:

$$\frac{\|\dot{\mathcal{X}}^{j+1} - \dot{\mathcal{X}}^{j}\|_F}{\|\dot{\mathcal{X}}^{j}\|_F}.$$

A consistent reduction in relative error is observed with successive iterations, confirming the numerical convergence of the proposed approach.

2) Sensitivity Analysis of Parameters β: Fig. 7 illustrates the impact of the regularization parameter β on the reconstruction performance of NTQTTV-1 and NTQTTV-2, evaluated on the *news* video dataset with a sampling rate of 0.2. For NTQTTV-1, β is varied from 0.001 to 5, and for NTQTTV-2, from 0.005 to 10. The results show that both models achieve stable and high PSNR and aSSIM scores over a broad range of β values. In particular, NTQTTV-1 performs robustly when $\beta \in [0.01, 1]$, while NTQTTV-2 maintains optimal performance for $\beta \in [0.01, 2]$. A gradual decline is observed only when β becomes excessively large or too small. These findings demonstrate the robustness of the proposed models with respect to β, and indicate that the parameter does not require overly precise tuning to achieve competitive results.

3) Ablation Study on the Nonlinear Transform: To validate the effectiveness of our proposed nonlinear transformation and to select the optimal activation function, we conducted an ablation study. We compared the performance of our NTQTTV1 and NTQTTV2 models using three distinct nonlinear functions: Sigmoid, Leaky ReLU, and the hyperbolic tangent (tanh). As a baseline, we also evaluated the models without any nonlinear transform, referred to as Linear NTQTTV1 and Linear NTQTTV2.

Table V presents the quantitative results (PSNR and aSSIM) for this comparison on the *news* video dataset. The results

TABLE V
THE PSNR/ASSIM VALUES OBTAINED WITH DIFFERENT NONLINEAR FUNCTIONS FOR NEWS. THE BEST NUMERICAL RESULTS ARE HIGHLIGHTED IN BOLD

Transfom Function	NTQTTV1			NTQTTV2		
	SR=3%	SR=5%	SR=10%	SR=3%	SR=5%	SR=10%
Linear	26.58 / 0.767	29.66 / 0.796	33.32 / 0.817	26.00 / 0.772	27.90 / 0.792	30.94 / 0.811
Sigmoid	28.41 / 0.782	30.84 / 0.802	33.36 / 0.816	26.20 / 0.775	28.15 / 0.794	31.24 / 0.813
Leaky ReLU	20.51 / 0.658	28.19 / 0.785	33.47 / 0.817	26.12 / 0.774	28.05 / 0.794	31.14 / 0.812
Tanh	**28.47 / 0.788**	**31.04 / 0.807**	**33.48 / 0.818**	**26.30 / 0.776**	**28.27 / 0.795**	**31.59 / 0.814**

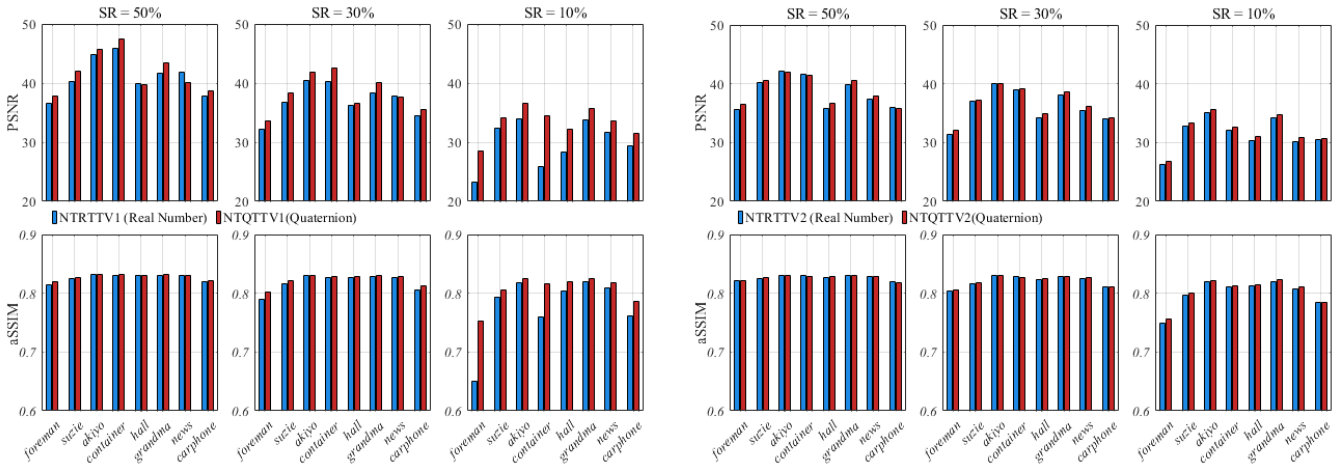

Fig. 8. Quantitative comparison for the ablation study on quaternion versus real-domain modeling.

clearly show that all models incorporating a nonlinear transform significantly outperform the linear baseline, which confirms the advantage of our core approach. Among the tested activation functions, the tanh function consistently yields the highest reconstruction quality. Based on these empirical findings, we adopt tanh as the chosen nonlinear transform for all subsequent experiments.

The superior performance of tanh can be attributed to its key mathematical properties. As a bounded, saturating nonlinearity, tanh maps the entire data range to a finite interval of $(-1, 1)$. This makes the low-rank recovery process more robust, especially in the context of image completion where large-magnitude values can arise from both the high dynamic range of known pixels and unstable estimates for missing entries during optimization. By compressing these extreme values, tanh prevents them from dominating the recovery process and allows the model to better focus on the underlying low-rank structure. Furthermore, its smooth, differentiable nature is highly beneficial for the stability of our gradient-based ADMM algorithm and is compatible with our Total Variation (TV) regularizer, as both favor smooth solutions. Finally, unlike the sigmoid function, its zero-centered output range of $(-1, 1)$ (compared to sigmoid's $(0, 1)$) avoids introducing a systematic bias into the iterative updates, leading to more stable and efficient convergence. In essence, tanh strikes an effective balance: its boundedness stabilizes the global recovery, while its smoothness and zero-centered output ensure a robust and efficient optimization process.

4) Quaternion Representation Vs. Real-Domain Modeling: To precisely quantify the advantage of the quaternion framework, we conducted an ablation study comparing our proposed NTQTTV1 and NTQTTV2 models against their direct real-domain counterparts, denoted NTRTTV1 and NTRTTV2. These baselines are structurally identical to our proposed models. They employ the same nonlinear transform, regularizers, and optimization scheme, with the sole difference that all quaternion-specific operations are replaced by their real-valued tensor equivalents, which treat the RGB channels as a separate tensor mode.

The quantitative results of this comparison on eight video datasets under SRs of 50%, 30%, and 10% are presented in Fig. 8. The results clearly demonstrate that both NTQTTV1 and NTQTTV2 consistently outperform their real-domain counterparts in most test cases in terms of both PSNR and aSSIM. More importantly, the performance gap between the quaternion and real-domain models widens dramatically as the sampling rate decreases. At SR = 50%, the NTRTTV models are competitive. However, as the problem becomes more ill-posed at SR = 30% and especially at SR = 10%, their performance degrades sharply, while our quaternion-based models maintain a much higher level of accuracy.

5) Discussion on Trade-Offs and Limitations: The primary advantage of our method is its ability to preserve complex inter-channel correlations via quaternion algebra, yielding superior results in applications where accuracy is paramount. However, this is balanced by two key limitations regarding

computational cost and the applicability of its core modeling assumption.

First, the sophisticated modeling is computationally intensive, making the method unsuitable for real-time applications like live video streaming. This challenge is compounded by the algorithm's exponential scaling with tensor order (as detailed in Section III-C), which limits its practicality for very high-dimensional datasets. Second, the method's core strength (its holistic treatment of channels) becomes a limitation when the underlying assumption of strong correlation is invalid. For instance, when applied to multi-channel scientific data with disparate spectral bands, the model may impose an unnatural correlation and consequently hinder performance.

V. Conclusion

This paper presents a unified quaternion-tensor low-rank completion model that jointly exploits the global low-rank structure, local smoothness, and nonlinear characteristics of multidimensional color images. To solve the resulting nonlinear and nonconvex optimization problem, a locally linear approximation strategy is employed within the ADMM framework, along with a convergence analysis. Extensive experiments on real-world color videos and light field images demonstrate that the proposed NTQTTV method consistently outperforms state-of-the-art techniques under high missing rates. As detailed in our discussion, the method's high computational cost and its core modeling assumption are key limitations for real-time applications. Future research will therefore focus on enhancing computational efficiency, particularly for the time-consuming QTSVT step. Promising directions include hardware acceleration by leveraging parallel architectures like GPUs and algorithmic advancements through the exploration of approximations such as randomized QSVD.

Acknowledgment

The authors would like to thank the editor and reviewers for giving them many comments and suggestions, which are of great value for improving the quality of this manuscript.

References

[1] J. A. Bengua, H. N. Phien, H. D. Tuan, and M. N. Do, "Efficient tensor completion for color image and video recovery: Low-rank tensor train," *IEEE Trans. Image Process.*, vol. 26, no. 5, pp. 2466–2479, May 2017.

[2] J. Miao and K. I. Kou, "Color image recovery using low-rank quaternion matrix completion algorithm," *IEEE Trans. Image Process.*, vol. 31, pp. 190–201, 2022.

[3] H. Wang, J. Peng, W. Qin, J. Wang, and D. Meng, "Guaranteed tensor recovery fused low-rankness and smoothness," *IEEE Trans. Pattern Anal. Mach. Intell.*, vol. 45, no. 9, pp. 10990–11007, Sep. 2023.

[4] K. Jiang et al., "Multi-scale progressive fusion network for single image deraining," in *Proc. IEEE/CVF Conf. Comput. Vis. Pattern Recognit. (CVPR)*, Jun. 2020, pp. 8343–8352.

[5] Y. Xiao, Q. Yuan, K. Jiang, Y. Chen, S. Wang, and C.-W. Lin, "Multi-axis feature diversity enhancement for remote sensing video super-resolution," *IEEE Trans. Image Process.*, vol. 34, pp. 1766–1778, 2025.

[6] J. Ren, H. Chen, T. Ye, H. Wu, and L. Zhu, "Triplane-smoothed video dehazing with CLIP-enhanced generalization," *Int. J. Comput. Vis.*, vol. 133, no. 1, pp. 475–488, Jan. 2025.

[7] S.-C. Pei and C.-M. Cheng, "A novel block truncation coding of color images using a quaternion-moment-preserving principle," *IEEE Trans. Commun.*, vol. 45, no. 5, pp. 583–595, May 1997.

[8] C. Huang, M. K. Ng, T. Wu, and T. Zeng, "Quaternion-based dictionary learning and saturation-value total variation regularization for color image restoration," *IEEE Trans. Multimedia*, vol. 24, pp. 3769–3781, 2022.

[9] Y. Chen, X. Xiao, and Y. Zhou, "Low-rank quaternion approximation for color image processing," *IEEE Trans. Image Process.*, vol. 29, pp. 1426–1439, 2020.

[10] Z.-H. He, X.-X. Wang, and Y.-F. Zhao, "Eigenvalues of quaternion tensors with applications to color video processing," *J. Sci. Comput.*, vol. 94, no. 1, p. 1, Jan. 2023.

[11] J. Miao, K. I. Kou, and W. Liu, "Low-rank quaternion tensor completion for recovering color videos and images," *Pattern Recognit.*, vol. 107, Nov. 2020, Art. no. 107505.

[12] J. Miao, K. I. Kou, L. Yang, and D. Cheng, "Quaternion tensor train rank minimization with sparse regularization in a transformed domain for quaternion tensor completion," *Knowl.-Based Syst.*, vol. 284, Jan. 2024, Art. no. 111222.

[13] J. Miao, K. I. Kou, H. Cai, and L. Liu, "Quaternion tensor left ring decomposition and application for color image inpainting," *J. Sci. Comput.*, vol. 101, no. 1, p. 1, Oct. 2024.

[14] J. Miao and K. I. Kou, "Quaternion tensor singular value decomposition using a flexible transform-based approach," *Signal Process.*, vol. 206, May 2023, Art. no. 108910.

[15] J. Liu, P. Musialski, P. Wonka, and J. Ye, "Tensor completion for estimating missing values in visual data," *IEEE Trans. Pattern Anal. Mach. Intell.*, vol. 35, no. 1, pp. 208–220, Jan. 2013.

[16] F. Zhang, J. Wang, W. Wang, and C. Xu, "Low-tubal-rank plus sparse tensor recovery with prior subspace information," *IEEE Trans. Pattern Anal. Mach. Intell.*, vol. 43, no. 10, pp. 3492–3507, Oct. 2021.

[17] X. Li, Y. Ye, and X. Xu, "Low-rank tensor completion with total variation for visual data inpainting," in *Proc. 31st AAAI Conf. Artif. Intell.*, San Francisco, CA, USA, S. Singh, and S. Markovitch, Eds., Palo Alto, CA, USA: AAAI Press, 2017, pp. 2210–2216.

[18] C.-Y. Ko, K. Batselier, L. Daniel, W. Yu, and N. Wong, "Fast and accurate tensor completion with total variation regularized tensor trains," *IEEE Trans. Image Process.*, vol. 29, pp. 6918–6931, 2020.

[19] D. Qiu, M. Bai, M. K. Ng, and X. Zhang, "Robust low-rank tensor completion via transformed tensor nuclear norm with total variation regularization," *Neurocomputing*, vol. 435, pp. 197–215, May 2021.

[20] Z.-Y. Wang, H. C. So, and A. M. Zoubir, "Low-rank tensor completion via novel sparsity-inducing regularizers," *IEEE Trans. Signal Process.*, vol. 72, pp. 3519–3534, 2024.

[21] B.-Z. Li, X.-L. Zhao, T.-Y. Ji, X.-J. Zhang, and T.-Z. Huang, "Nonlinear transform induced tensor nuclear norm for tensor completion," *J. Sci. Comput.*, vol. 92, no. 3, p. 83, Sep. 2022.

[22] Y.-S. Luo, X.-L. Zhao, T.-X. Jiang, Y. Chang, M. K. Ng, and C. Li, "Self-supervised nonlinear transform-based tensor nuclear norm for multi-dimensional image recovery," *IEEE Trans. Image Process.*, vol. 31, pp. 3793–3808, 2022.

[23] L. Luo, Z. Tu, J. Lu, C. Wang, and C. Xu, "A nonlinear high-order transformations-based method for high-order tensor completion," *Signal Process.*, vol. 225, Dec. 2024, Art. no. 109514.

[24] G.-W. Yang, L. Yang, T.-X. Jiang, G. Liu, and M. K. Ng, "DELTA: Deep low-rank tensor representation for multi-dimensional data recovery," *IEEE Trans. Pattern Anal. Mach. Intell.*, vol. 48, no. 3, pp. 3018–3035, Mar. 2026.

[25] W. R. Hamilton, "Ii. On quaternions; or on a new system of imaginaries in algebra," *London, Edinburgh, Dublin Philos. Mag. J. Sci.*, vol. 25, no. 163, pp. 10–13, 1844.

[26] F. Zhang, "Quaternions and matrices of quaternions," *Linear Algebra Appl.*, vol. 251, pp. 21–57, Jan. 1997.

[27] J. Pan and M. K. Ng, "Block-diagonalization of quaternion circulant matrices with applications," *SIAM J. Matrix Anal. Appl.*, vol. 45, no. 3, pp. 1429–1454, Sep. 2024.

[28] J. Wang, Y. Chen, R. Chakraborty, and S. X. Yu, "Orthogonal convolutional neural networks," in *Proc. IEEE/CVF Conf. Comput. Vis. Pattern Recognit. (CVPR)*, Jun. 2020, pp. 11502–11512.

[29] T. Parcollet et al., "Quaternion recurrent neural networks," in *Proc. 7th Int. Conf. Learn. Represent. (ICLR)*, New Orleans, LA, USA, 2019, pp. 1–19.

[30] A. L. Maas, A. Y. Hannun, and A. Y. Ng, "Rectifier nonlinearities improve neural network acoustic models," in *Proc. ICML*, vol. 30, no. 1, Atlanta, GA, USA, 2013, p. 3.

[31] S. Boyd, "Distributed optimization and statistical learning via the alternating direction method of multipliers," *Found. Trends Mach. Learn.*, vol. 3, no. 1, pp. 1–122, 2010.

[32] L. Yang, K. I. Kou, J. Miao, Y. Liu, and P. M. Hoi, "Quaternion tensor completion with sparseness for color video recovery," *Appl. Soft Comput.*, vol. 154, Mar. 2024, Art. no. 111322.
[33] D. Xu and D. P. Mandic, "The theory of quaternion matrix derivatives," *IEEE Trans. Signal Process.*, vol. 63, no. 6, pp. 1543–1556, Mar. 2015.
[34] Y. Wang, J. Yang, W. Yin, and Y. Zhang, "A new alternating minimization algorithm for total variation image reconstruction," *SIAM J. Imag. Sci.*, vol. 1, no. 3, pp. 248–272, Jan. 2008.
[35] E. Hitzer, "Quaternion Fourier transform on quaternion fields and generalizations," 2013, *arXiv:1306.1023*.
[36] J. Zeng, S. Lin, Y. Yao, and D. Zhou, "On ADMM in deep learning: Convergence and saturation-avoidance," *J. Mach. Learn. Res.*, vol. 22, p. 199:1–199:67, Jan. 2021.
[37] D. Xu, C. Jahanchahi, C. C. Took, and D. P. Mandic, "Enabling quaternion derivatives: The generalized HR calculus," *Roy. Soc. Open Sci.*, vol. 2, no. 8, Aug. 2015, Art. no. 150255.
[38] Y. Xu and W. Yin, "A block coordinate descent method for regularized multiconvex optimization with applications to nonnegative tensor factorization and completion," *SIAM J. Imag. Sci.*, vol. 6, no. 3, pp. 1758–1789, Jan. 2013.

Liqiao Yang received the M.S. degree in mathematics from the University of Electronic Science and Technology of China, Chengdu, China, in 2020, and the Ph.D. degree in mathematics from the University of Macau, China, in 2024. She is currently a Postdoctoral Researcher with the Southwestern University of Finance and Economics. Her current research interests include quaternion modeling and algorithms for high-order data recovery.

Yexun Hu (Graduate Student Member, IEEE) received the M.S. degree from the School of Computing and Artificial Intelligence, Southwestern University of Finance and Economics (SWUFE), Chengdu, China, in 2023, where he is currently pursuing the Ph.D. degree.

His research interests include tensor modeling and algorithm for high-order data recovery.

Tai-Xiang Jiang (Member, IEEE) received the B.S. and Ph.D. degrees in mathematics and applied mathematics from the University of Electronic Science and Technology of China (UESTC), Chengdu, China, in 2013 and 2019, respectively. He is currently a Professor with the School of Computing and Artificial Intelligence, Southwestern University of Finance and Economics. His research interests include sparse and low-rank modeling, tensor decomposition, and multi-dimensional image processing.

Yimin Wei received the B.S. degree in computational mathematics from Shanghai Normal University, Shanghai, China, in 1991, and the Ph.D. degree in computational mathematics from Fudan University, Shanghai, in 1997. He is currently a Full Professor with the School of Mathematical Sciences, Fudan University. He is the author of more than 200 technical journal articles and five monographs published by Elsevier, Springer, World Scientific, EDP Science, and Science Press. His current research interests include multilinear algebra and numerical linear algebra with their applications.

Guisong Liu (Member, IEEE) received the B.S. degree in mechanics from Xi'an Jiaotong University, Xi'an, China, in 1995, and the M.S. degree in automatics and the Ph.D. degree in computer science from the University of Electronic Science and Technology of China, Chengdu, China, in 2000 and 2007, respectively.

He was a Visiting Scholar with Humbolt University, Berlin, Germany, in 2015. Before 2021, he was a Professor with the School of Computer Science and Engineering, University of Electronic Science and Technology of China. He is currently a Professor and the Dean of the School of Computing and Artificial Intelligence, Southwestern University of Finance and Economics, Chengdu. He has field over 20 patents, and published over 70 scientific conference and journal articles. His research interests include pattern recognition, neural networks, and machine learning.

Michael K. Ng (Senior Member, IEEE) received the B.Sc. and M.Phil. degrees from The University of Hong Kong, in 1990 and 1992, respectively, and the Ph.D. degree from The Chinese University of Hong Kong in 1995. He was a Research Fellow with the Computer Sciences Laboratory, The Australian National University, from 1995 to 1997, and an Assistant/Associate Professor with The University of Hong Kong from 1997 to 2005. He was a Professor/Chair Professor with the Department of Mathematics, Hong Kong Baptist University, from 2006 to 2019. He was a Chair Professor with the Research Division of Mathematical and Statistical Science, The University of Hong Kong, from 2019 to 2023. He is currently a Chair Professor of mathematics and a Chair Professor of data science with Hong Kong Baptist University. His research interests include bioinformatics, image processing, scientific computing, and data mining. He is selected for the 2017 Class of Fellow of the Society for Industrial and Applied Mathematics. He was the recipient of the Feng Kang Prize for his significant contributions in scientific computing. He serves on the Editorial Board members of several international journals